Investigation of thermal properties and alternative sensor integration concepts for the CBM-MVD

Untersuchungen von Wärmeleiteigenschaften und alternativen Sensorintegrationskonzepten für den CBM Mikro-Vertex-Detektor

Abschlussarbeit

zur Erlangung des Mastertitels

"Master of physics"

vorgelegt am Fachbereich 13

der Johann-Wolfgang-Goethe-Universität

in Frankfurt am Main

von

Fabian Hebermehl

aus Steinbach(Ts.)

Frankfurt (2023)

Johann Wolfgang Gothe-Universität Frankfurt am Main

Fachbereich Physik

Masterarbeit zur Erlangung des wissenschaftlichen Titels Master of Science

---

Erstgutachter:

Prof. Dr. Joachim Stroth

Zweitgutachter:

Dr. Christian Müntz

Abgabedatum:

19.10.2023

Abstract

The **M**icro **V**ertex **D**etector is part of the CBM experiment for FAIR SIS 100. It encompasses four stations placed in vacuum behind the target to measure tracks of charged particles emitted from heavy ion collisions and proton induced reactions. Each station is comprised of four quadrants housing thinned MIMOSIS sensors placed front-and backside on a carrier which provides structural/mechanical support and evacuates heat produced by the sensors. This thesis was inspired by the need to qualitatively formalize the production yield of the module construction process as well as assess options to improve the mechanical concept w.r.t. production yield, taking into account thermal performance and material budget. For this purpose three different concepts and two materials of deidcated high-performance have been evaluated. A simulation software was tuned and tested based on systemic measurements to understand if reliable predictions can be made.

Contents

Abstract **i**

1 Background **1**

1.1 Heavy Ion Collisions 2
1.2 FAIR and CBM Experiment 4
1.3 Micro Vertex Detector 6
1.3.1 The MIMOSIS Sensor 6
1.3.2 Secondary Vertex Reconstruction 7
1.4 Constraints of MVD Construction 10
1.5 MVD Construction 10
1.6 MVD Quadrant 10
1.7 Goal and Structure of Thesis 14

2 Construction Options and Materials **15**

2.1 Description of Options 15
2.2 Production Yield 16
2.2.1 Reworking the MVD Modules 17
2.2.2 Baseline 18
2.2.3 Thinned Baseline 20
2.2.4 Ladders 20
2.2.5 2xOnesided TPG 21
2.2.6 PGS And RVC Composite 22
2.2.7 Discussion of Production Yield 23
2.3 Material discussion 27
2.3.1 Thermal Pyrolytic Graphite 28
2.3.2 Pyrolitic Graphite Sheets 28

2.3.3 Reticulated Vitreous Carbon 29

3 Thermal Testing and Validation **31**

3.1 Test Setup “UFO” 32

3.1.1 Cooling Loop 33

3.1.2 Pt100 Sensors 34

3.1.3 IR Camera 36

3.1.4 Other Sensors 37

3.1.5 Kapton Heater 37

3.1.6 Thermal Conductivity 38

3.1.7 Calculating Temperature Difference of Baseline 39

3.1.8 Error Discussion 40

3.2 Error calculations 45

3.2.1 Validation of UFO Setup 46

3.3 Material Validation 49

3.3.1 Results 51

3.4 Thermal Simulations using ThSim 55

3.4.1 Aligning Simulation Parameters to Reference Measurements 55

3.4.2 Simulations 57

3.4.3 Comparison to High Fidelity Simulations 60

3.5 Carrier Measurement 62

3.5.1 Discussion Carrier Experiment 63

4 Summary **69**

5 Appendices **73**

5.1 Bent TPG Measurement 73

Bibliography **75**

List of Figures

1.1 QCD phase diagram sketch. 3
1.2 Interaction rates of heavy-ion experiments. 4
1.3 CBM/MVD CAD view 5
1.4 Idealized two layer detector example 7
1.5 Momentum-Radiation length diagram for two station detector 8
1.6 Momentum distribution of fireball spectra 9
1.7 MVD CAD half station schematic 11
1.8 MVD module cross section 12
1.9 MVD construction guide (up to half station) 13

2.1 ThSim visual representation of carrier construction options 16
2.2 MVD Radiation length gemometry c 18
2.3 Baseline Assembly flow 19
2.4 Ladders Assembly flow 21
2.5 Double sided Assembly flow 22
2.6 Rolling throughput yield assumption of Baseline and 2xOnesided 26
2.7 Thermal Figure of Merit for Different Materials for the MVD 27
2.8 Manufacturer specifications and comparison of PGS. 29
2.9 Photographs of the materials of interest in this thesis. 30

3.1 Photo of UFO with comments on where components are. 32
3.2 Cooling loop and sensor UFO flowchart 33
3.3 Sensor histograms on carrier and inlet 35
3.4 A simple Bolometer schematic. 36
3.5 Corrections of IR camera 37
3.6 Graphic depicting thermal conductivity. 38

3.7 Computed thermal difference component to component of a module station c . . 39
3.8 Thermal equalization over time of a carrier sample 41
3.9 Thermal difference between top and bottom of a TPG carrier 42
3.10 Power input of environment computed vs. measured 44
3.11 Infrared picture of a 3 W measurement of copper. 46
3.12 Photograph copper sample 47
3.13 ΔT on copper. 48
3.14 Thermal conductivity over averaged temperature. 48
3.15 Photographs of TPG Sample 50
3.16 Photograph PGS/RVC Sample 50
3.17 Measured Temperature difference vs. Power TPG & PGS 51
3.18 Thermal conductivity vs. average temperature TPG & PGS 52
3.19 Thermal conductivities as measured compared to each other 53
3.20 Thermal conductivity of TPG measured by [HMK02] 54
3.21 TPG strip lined up to ThSim-based simulations. 56
3.22 Station c simulations alternative designs. 58
3.23 Station c simulations. 59
3.24 Thermal conductivity comparison of simulated carrier options. 60
3.25 Station geometry c simulations done in Autodesk Inventor Nastran. 61
3.26 Baseline and thin carrier options test sample images. 62
3.27 Thermal conductivity comparison of simulated carrier options and measurements. 63
3.28 1/x correction plot example 65
3.29 Comparison of possible corrections to measurements. 66

4.1 ThSim visual representation of carrier construction options 69

5.1 Damage on bent TPG. 73
5.2 Bent TPG thermal image 74

List of Tables

1.1 Constraints of the MVD. 10

1.2 MVD station geometries a b and c properties. 12

2.1 Carrier design options 15

2.2 Chosen carrier material properties 30

3.1 Variables values and constants for modified Stefan Boltzmann 43

3.2 Copper sample Thermal conductivity results. 48

3.3 Parameters for the different test strip measurements 49

3.4 Thermal conductivity results for TPG and PGS 53

3.5 ΔT comparison between TPG strip measured and simulated 56

3.6 ΔT comparison between each simulated option. 59

3.7 ΔT comparison of ThSim and Inventor Nastran 61

3.8 Carrier measurement experiment parameters. 62

3.9 λcomparison for carrier measurements with λused in simulation 67

4.1 Comparison of ΔT of simulations with measurements for baseline and thinned basline. 71

Background 1

To describe the universe‘s building blocks, nuclear physics experiments conducted throughout the 20th and 21st century have been used to create and solidify the Standard Model of particle physics. This standard model describes electromagnetic, weak and strong interaction. The strong interaction is described using Quantum Chromo Dynamics (QCD) and governs interactions between quarks and gluons. Inside QCD the **running** coupling constant α_s plays a key role. It decreases with either increasing momentum transfer or decreasing distances between the interacting particles. This results in two regimes, labeled confinement and asymptotic freedom. Quarks and gluons cannot exist as free particles, they are typically **confined** inside structures like Protons and Neutrons. At high momentum transfers or short distances, this confinement of quarks and gluons weakens by orders of magnitude. This regime is known as Asymptotic freedom, a state of quasi-free quarks and gluons called a Quark Gluon plasma (QGP). The phase diagram of the QCD (fig. 1.1) suggests, that to reach the QGP temperature and compression of nuclear matter can be used. For the CBM the lower temperature region with higher density is of interest as this region may include a critical point. To probe this region multi differential cross sections of e.g. rare particles or fluctuations are the focus. To ensure a high statistic, the collision rates of the experiment need to be high. This influences all decisions made for the CBM-MVD.

1.1 Heavy Ion Collisions

Heavy-ion collisions are achieved in fixed-target and collider experiments. In a fixed-target experiment the beam of heavy ions is aimed at a stationary target. During the collisions with this target, a short lived, hot and dense state of matter is created, called the fireball. The same can be done with collider experiments, where two beams of heavy ions are brought together inside a detector and interact. Fixed-target collisions require a Lorentz boost to reach the momentum rest frame [1] and compress the acceptance angle into a forward cone requiring high granularity in the sensors, while in collider experiments the momentum rest frame is the laboratory reference frame.

One well-known facility for collider type experiments is the Large Hadron Collider (LHC) at the European Organization for Nuclear Research (CERN). Experiments that are conducted at LHC include ALICE [A+08b], ATLAS [A+08a] and CMS [C+08]. They probe the high temperature and low to zero net-baryon density state of QCD.

[1] A momentum rest frame is the reference frame of the particle if it's momentum were at 0.

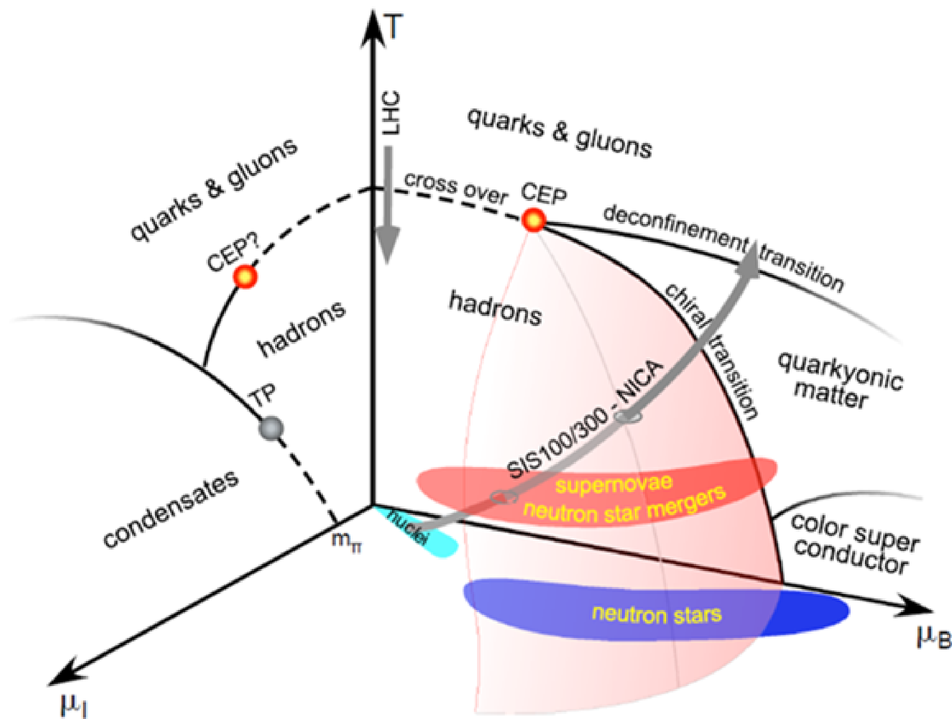

FIGURE 1.1 –

A QCD phase diagram sketch showing theoretical predictions of nuclear matter as function of temperature, baryon-chemical and isospin-chemical potential[Bra17].

The future Compressed Baryonic Matter Experiment at the SIS100 accelerator at the **F**acility for **A**ntiproton and **I**on **R**esearch FAIR is a detector under construction to probe high baryon densities and low to moderate temperatures with unprecedented interaction rates [Hö07]. This enables probing of a region of interest to contemporary nuclear physics of the QCD phase diagram (fig. 1.1) possibly containing a first-order phase transition and a critical point. CBM is a fixed-target experiment with a high collision rate. This translates into constraints for the detectors of high clock speeds, high granularity of sensors as well as radiation hardness.

1.2 FAIR and CBM Experiment

FAIR is currently under construction in the vicinity of present-day GSI. Its accelerator ring SIS100 will accelerate proton and heavy ion beams as required with energies of 5-11 AGeV for Au+Au collisions [SBB+20]. The **C**ompressed **B**aryonic **M**atter eExperiment (CBM) utilizes this capability to probe the QCD phase diagram at high net-baryon densities and low-to-medium temperatures. At Au+Au collisions at beam energies of 5-10 AGeV, simulations predict densities of 6 to 8 times saturation density ρ_0 inside the center of the fireball [ABC+07, FHK+11].

A lot of the processes of interest have low production cross sections thus a high interaction rate is required for sufficient statistics. Here CBM is designed to run at interaction rates of **100 kHz** up to **10 MHz**.

This puts CBM orders of magnitude above other existing and planned heavy-ion experiments (see fig. 1.2).

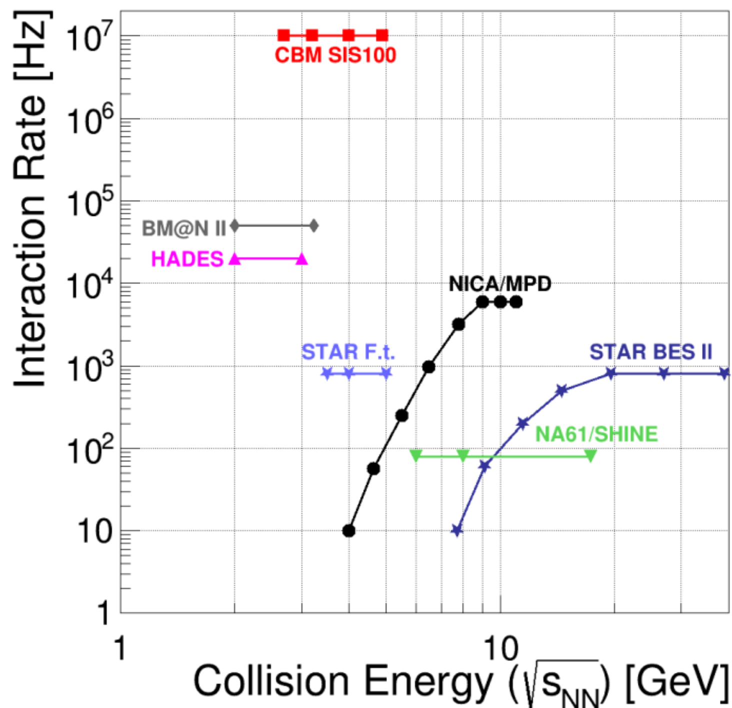

Figure 1.2 –

Interaction rates of planned and existing heavy-ion experiments as function of center-of-mass energy [SD22].

The CBM experiment is composed of several detectors working together as seen in fig. 1.3. The main detector of CBM is the STS, with the MVD being a sub detector. The MVD will be discussed below.

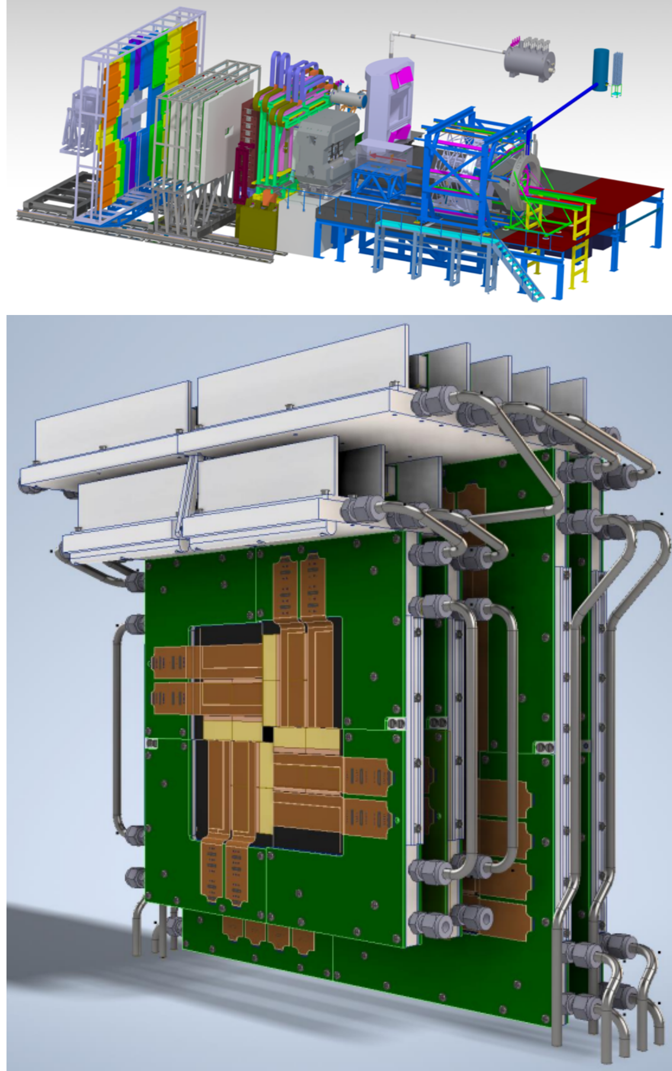

FIGURE 1.3 –
Top: CAD view of the CBM experiment [col23]. From right to left: Hades, Superconducting magnet, inside it are the MVD and STS, afterwards the MuCh in measuring position and RICH in parking position, further the TRD and ToF. Behind the Tof is the ECal.
Bottom: CAD view of the MVD from the front. The 4 station positions are shown moved active position [F.M].

1.3 Micro Vertex Detector

The **M**icro **V**ertex **D**etector (MVD) was initially predicted to enable secondary vertexing of open-charm D mesons emitted in violent heavy ion collisions in the SIS-300 energy regime, using CMOS pixel sensors, with a secondary vertexing precision of better than 70 microns [SD22]. Meanwhile, only SIS-100 will become available, i.e. serving a maximum kinetic energy of Au-ions of about 10 AGeV. In addition, the MVD is suited for dilepton spectroscopy and hyperon decay reconstruction, complimenting the STS by extending the acceptance of CBM down to momenta of 300 MeV/c. To achieve this acceptance, the MVD is constrainted by a low material budget, requiring it to run in a vacuum to minimize material between it and the target (see ch. 1.3.2. The high collision rate requires a high radiation hardness of the chosen components, in particular the sensors.

1.3.1 The MIMOSIS Sensor

The chosen sensor for the MVD is the CMOS Pixel sensor (CPS) MIMOSIS. The aim with MIMOSIS is a pixel granularity of ~ 5 µm and a collision rate of 100 kHz [SD22]. The sensor geometry is given as 31.150 × 17.250 mm^2, thinned to a thickness of 50 µm (see [SD22]). A power density of ~50-100 $\frac{mW}{cm^2}$ is assumed based off the high readout speed and simulations done for the sensor. Potentially the power density can fall to 42 $\frac{mW}{cm^2}$ (see [F.M19]), but for this thesis a higher value is used to stay on the conservative side. Each chip contains four matrices of pixel with high granularity. To keep a high S/N-ratio and reduce radiation induced noise, the sensor needs to be cooled down to below zero. Additionally the temperature difference across a sub-sensor matrix has to be held low so in order to minimize temperature-driven non uniformity in the pixel response. **For the temperature difference, a benchmark of $\Delta T = 10$ K assumed in this thesis.**

1.3.2 Secondary Vertex Reconstruction

To understand why close proximity to the fireball is desired, one looks at how secondary vertices are reconstructed. See fig. 1.4 and references [Wer06, Tis15] for detail. Equation 1.2, modelling this interaction, is deduced from particle collider geometry for two stations in this case. It is composed of a geometric component (first term) based on the geometry of the detector and the sensor granularity and a multiple scattering component (second term).

$$\sigma_{SV}^2 = \frac{\sigma_{Geo}}{\sigma_{MS}} \tag{1.1}$$

$$\sigma_{SV}^2 = \frac{\sigma_1^2 r_2^2 + \sigma_2^2 r_1^2}{(r_2 - r_1)^2} + \frac{\theta_{ms} r_1^2}{cos^4(\theta)} \tag{1.2}$$

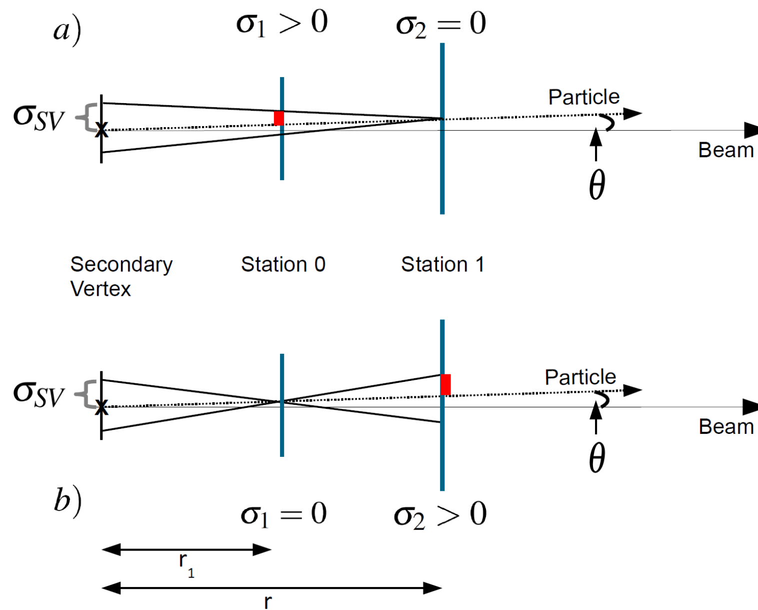

FIGURE 1.4 –

An idealized schematic of a two layer detector system [Tis15]. Diagram a) shows a detector where layer 2 is ideal ($\sigma_2 = 0$). Diagram b) conversely shows a detector with an ideal layer 1 ($\sigma_1 = 0$). Θ is the angle of the particle impacting onto the detector. The particle tracks are given as straight tracks. The uncertainty resulting from geometry (distances, spatial precision) perpendicular to the beam axis σ_{SV} is indicated. The material of station 0 adds (quadratically) a multiple scattering contribution. The red squares show the position error on the station.

Here $\sigma_{1,2}$ denote the error in position measurements for the first and second detector station and is based on the pixel pitch of the sensor as $\sigma_1 = \sigma_2 = \frac{Pitch^2}{\sqrt{12}}$. Θ denotes the impact angle of the particle. for a sufficiently small angle of Θ the cosine moves towards 1 and as such multiple

[2]This case for the pixel pitch applies in this case as there is no charge sharing.

scattering is left in the second term in eq. 1.2. Multiple scattering itself is defined as eq. 1.3, where $\beta = v/c_0$, p being the momentum, c the speed of light and z the charge of the particle.

$$\Theta_{ms} = \frac{13.6MeV}{\beta pc} z\sqrt{x/X_0}[1 + 0.038ln(x/X_0)]. \tag{1.3}$$

Of importance is that Θ_{ms} is tied to the material budget x/X_0 by a square root. The material budget is a fraction defined by the thickness of material divided by its radiation length. Radiation length X_0 characterizes the amount of matter an electron has to travel through to lose 1/e of its energy [WO22] which is measured in g/cm^2. To make it compatible with material budget, X_0 is multiplied with the materials density ρ to remove the mass from X_0

For the design of MVD it is important to understand which of the two components in eq. 1.2 dominates the equation. To visually present this question, fig. 1.5 compares material budget to the laboratory momentum. The graph is created by setting the geometric and multiple scattering part of eq. 1.2 equal ($\frac{\sigma_1^2 r_2^2+\sigma_2^2 r_1^2}{(r_2-r_1)^2} = \frac{\theta_{ms} r_1^2}{cos^4(\theta)}$), creating a transition line from geometry dominated momentum to multiple scattering dominated momentum.

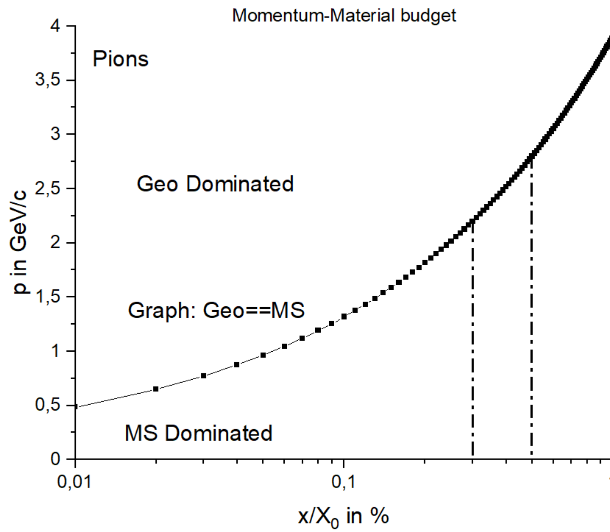

Figure 1.5 –

A model graph showing the momentum in GeV/c against the radiation length of two stations only for pions. The station parameters are r_1=8 cm, r_2=12 cm, $\sigma_{1,2}$=8 μm, small impact angle θ_π. "Geo dominated" denotes the area above the curve where the geometric part of eq. 1.2 is larger than the multiple scattering component. Conversely "MS dominated" denotes the area where multiple scattering dominates the equation.

The MVD's tracking configuration values is used for the geometry (r_1=8 cm, r_2=12 cm, $\sigma_{1,2}$=8 µm). The MVD's given material budget is 0.3-0.5% per station as given in [SD22]. This low material budget is crucial for MVD due to the momentum distribution expected at SIS100's projected collision energies (see fig. 1.6).

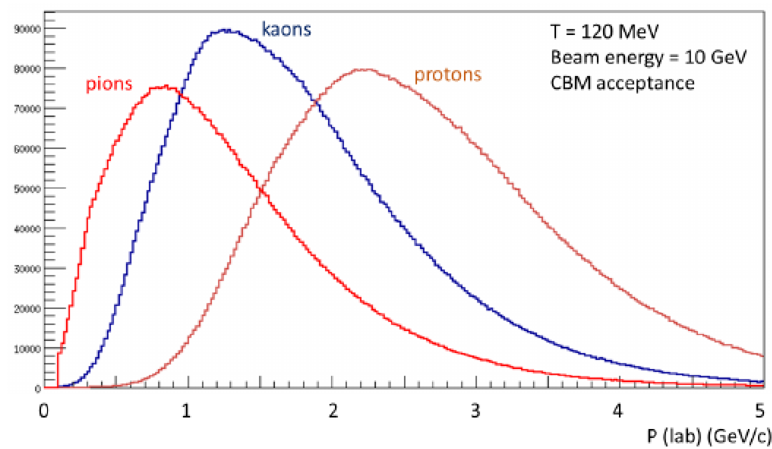

Figure 1.6 –

Momentum distributions of fireball spectra assuming a thermal source of $T = 120\,MeV$ *at* $E_{beam} = 10\,AGeV$ *[C.M].*

Comparing fig. 1.5 and 1.6 multiple scattering dominates the majority of the momentum distribution for pions. To minimize this material budget between the MVD and the target, no vacuum window is used and as such places the MVD in a moderate vacuum of 10^{-4} mbar.

Due to the operation of the MVD in vacuum and its requirement for low radiation length, the only option left for cooling the sensors in the acceptance is heat transfer through solids.

1.4 Constraints of MVD Construction

This gives a list of constraints either given by the construction or the results of the physics cases.

Constraint	Result
Radiation length	0.3-0.5 x/X_0, No vacuum window
Vacuum (10^{-4} mbar)	Only thermal conductivity in acceptance
Inactive sensor area	Double sided sensor placement
Sensor power density	70-100 $\frac{mW}{cm^2}$
ΔT over carrier (benchmark)	~10 K
Mechanical stiffness	At least one component with high Youngs Modulus E
Thermal expansion	CTE mismatch as low as possible
Magnetic field	Momentum modification between stations
Radiation field Strong, localized, inhomogenous	Radiation hard components

Table 1.1 –
A table listing the different constraints for the MVD, either given by material or the physics case.

1.5 MVD Construction

The MVD is comprised of four stations in either tracking or vertexing configuration, which influences the distance between each station. Each station is comprised of two half stations so the MVD can be moved out of the beamline for higher collision rate experiments the MVD would not be able to handle due to radiation concerns. Each half station is built out of two quadrants, made up of a heatsink and a module comprised of the carrier, **F**lex **P**rint **C**ircuitry (FPC) cables and the sensors.

1.6 MVD Quadrant

A quadrant of the MVD (see fig. 1.3 bottom) is made up of a heatsink (grey) and a module built of the CMOS sensors (orange), **F**lex **P**rint **C**ircuitry cables (FPC, green) and the thermal/mechanical carrier (light grey), see fig. 1.7 for detail.

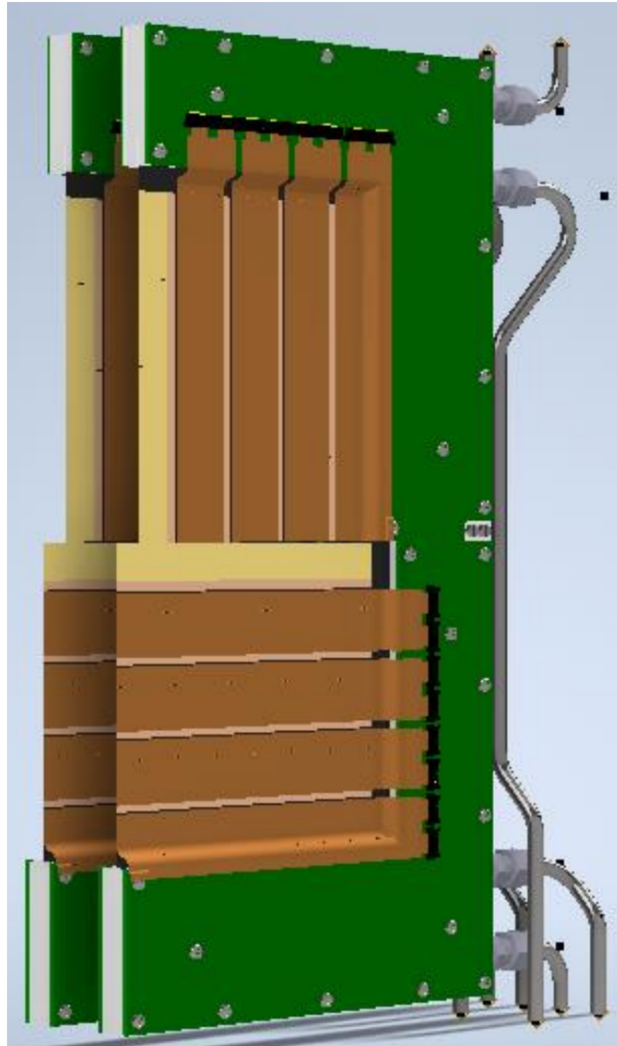

Figure 1.7 –
CAD design of the MVD half station geometry c [F.M]. It consists of two quadrants made of two modules (sensors (beige), FPC cables (brown) and carrier (dark grey), clamped in a heatsink (light grey). The heatsink is connected to the cooling system and the cables are connected to R/O, slow control and biasing equipment.

Depending on the quadrant geometry (a, b, c), it uses either **p**yrolitic **C**hemical **V**apour **D**eposited (pCVD) diamond (see [SD22], quadrant geometry a) or TPG (quadrant geometry b, c), **T**hermal **P**yrolitic **G**raphite [SD22]). Both materials are mechanically stable, thermal high performance materials with a high radiation length X_0. Each station contains a number of sensors split between front and back, to cover each sides inactive sensor area (see fig. 1.8). Each configuration uses a different amount of sensors and carrier size (see table 1.2).

Station geometry	a	b	c
Inner radius (beamhole) [mm]	5.4	5.4	10.4
Active area [cm^2]	33.0	130.6	455.1
no. of sensors front+back side	4+4	16+16	64+48
Module carrier dimensions [mm^2]	51.0 x 59.6	81.9 x 85.7	129.0 x 143.9
Carrier material	pCVD diamond	TPG	TPG

Table 1.2 –
The baseline properties of station geometries a b and c as given in the TDR [SD22]. The given numbers describe a complete station made up of four quadrants.

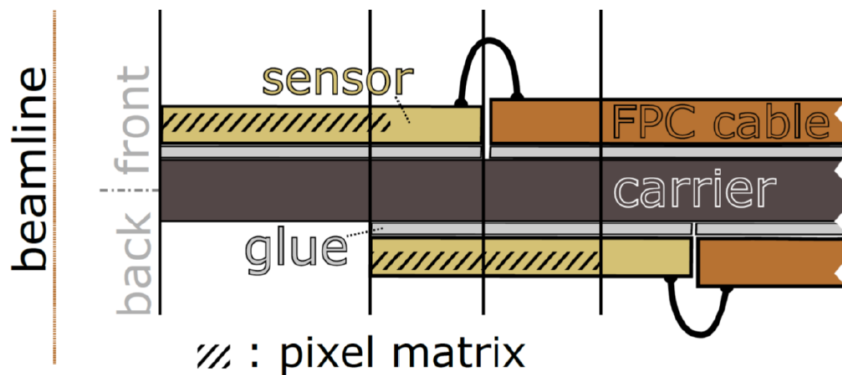

Figure 1.8 –

Cross section [SD22] of a module. In grey/brown: the carrier material. Onto it, sensors (yellow) are glued, so that the pixel matrices (shaded) overlap the inactive areas of the opposite sensors. between the sensors and the carrier is a layer of glue (grey). The FPC cables (orange) are wirebonded to the sensors.

The sensors are glued onto front and back of a carrier and bonded to FPC cable based readout/biasing. These copper based cables then connect to frontend boards outside the acceptance, situated on the heatsink. The sensor carrier is clamped into the heatsink. Inside the aluminium based heatsink are machined channels optimized for coolant based heat transfer. Originally it was designed to work with a single-phase, low-viscosity, liquid coolant based on Novec-649 [3M09] but new EU regulations requires a new coolant due to environmental concerns. This assembly constitutes one quadrant of a station. For a full assembly step by step demonstrated based on gemoetry A, look at fig. 1.9.

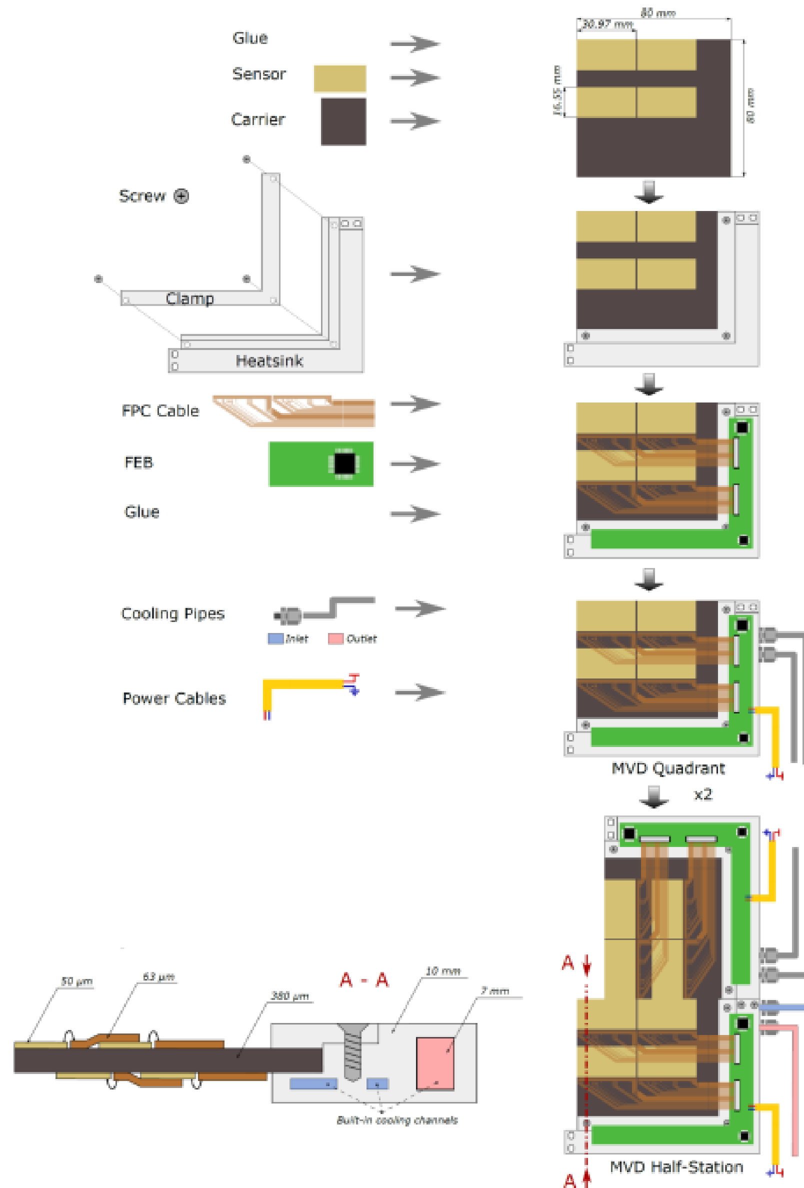

FIGURE 1.9 –

Assembly of a half station for MVD geometry a [SD22]. This thesis focuses on the initial step for station geometry c.

1.7 Goal and Structure of Thesis

As described in ch. 1.6 the construction of a quadrant/module is complex and contains a large amount of individual pieces with potential issues in production yield and reworking. Stemming from this the goal of the thesis is to compare different carrier concepts for their viability in terms of production yield and efficacy such as increases in modularity and reduction of sensors per module. This will be combined with a thermal capability test of the already chosen material for the MVD, TPG and a possible composite option of RVC and PGS that conceptually promises an appreciable reduction in material budget at similar thermal performance. The materials will be tested, the resulting thermal conductivity measurements used to tune thermal simulation programs. These tuned programs are then used to simulate the different module concepts, after which two options are measured in their thermal performance to compare if a tuned simulation can predict or replicate the measured performance.

Construction Options and Materials 2

2.1 Description of Options

The stated goal is to devise concepts that could increase production yield/modularity while keeping the thermal performance at a temperature difference of $\Delta T \sim 10\,\mathrm{K}$ across the carrier at 70-100 $\frac{\mathrm{mW}}{\mathrm{cm}^2}$ and the material budget x/X_0 below 0.5 % averaged of the MVD station. To increase modularity, several concepts outlined in table 2.1 are introduced.

	Baseline	thin Baseline	2xOnesided	Ladders	PGS/RVC
No. of modules	1		2	4	2
No. of sensors per module	28		16/12	7	16/12
Carrier thickness in µm	380	250	150	380	2040
Cross section one module	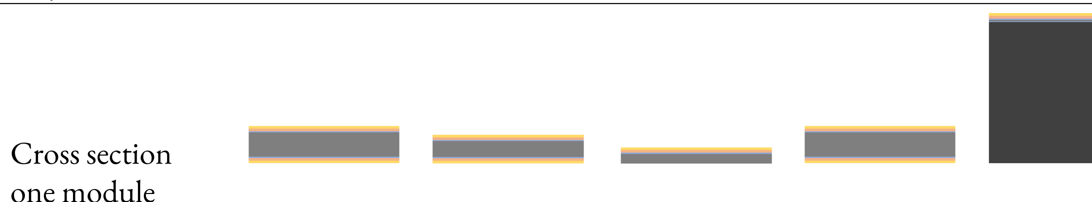				

Table 2.1 –
A short list of the conceptual properties of the different options to be evaluated. The cross section of each option is displayed at the bottom. Yellow denotes sensor and FPC cables, light blue glue, light grey TPG/PGS and dark grey RVC.

One potential aggressive option is a composite of **P**yrolitic **g**raphite **s**heets (PGS) and **R**eticulated **v**itreous **c**arbon foam (RVC). It is chosen due to potentially large savings in material budget.

Additionally a conservative option of thinning the baseline to 250 μm thick TPG is also evaluated. For each concept, a visual representation was created using ThSim in figure 2.1.

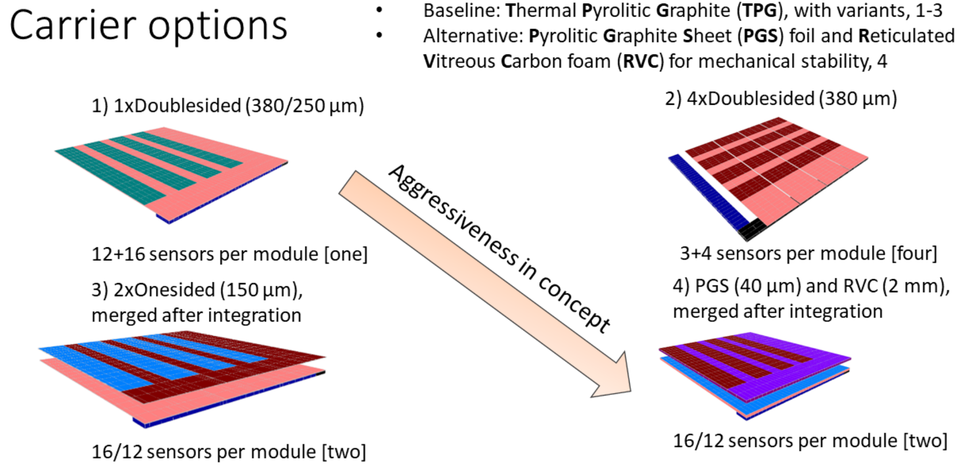

Figure 2.1 –

Visual representation of options discussed in this thesis, done with ThSim. Top left: Baseline and thinned baseline (1xDoublesided). Top right: Ladders (4xDoublesided). Bottom left: 2xOnesided TPG. Bottom Right: PGS/RVC composite (2xOnesided). The top and bottom are separated to show the idea behind the 2xOnesided concepts.

2.2 Production Yield

Production yield in the industry denotes the percentage of a product X that is successfully produced in a number of steps in relation to the total number N of produced products.

$$FTY = Y = \frac{X}{N} \tag{2.1}$$

$$RTY = \prod_{i}^{M} Y_i \tag{2.2}$$

Equation 2.1 can be referred to as the "First Time Yield" (FTY) of a process in a production line. Assuming independent probability, each step can be multiplied into the rolling throughput yield RTY (eq. 2.2). If a product is reworked during a step of the process, the equation of that step changes to equation 2.3, [Han].

$$Y_{rework} = \frac{X \cdot Y_g + X \cdot (1 - Y_g) \cdot (Y_r)}{N} \tag{2.3}$$

In eq.2.3 Y_g denotes the yield of good units, Y_r denotes the yield of reworked units. This allows for a description of the entire production lines yield after reworking.

For the MVD, this number is crucial as each quadrant in the larger stations require a large amount of MIMOSIS sensors. Thus, the successful production of modules is paramount to keep the waste as low as possible, as having to throw away an entire built module due to one fouled sensor would quickly drive the production costs up.

Additionally no quantitative numbers exist of produced good units compared to a total number of produced units for the MVD, the discussion as such will be focused on the qualitative up- and downsides of different options. For this, the equation 2.1 will be defined in a more granular way in equation 2.4. Here, the production yield of a module is defined as the yield of sensor integration I, FPC cable bonding B, FPC cable gluing G and additional mechanical steps M under assumption of independent processes and steps.

$$RTY_{Module} = \prod_{h,i,j,k}^{l,n,m,o} I_i \cdot B_j \cdot M_k \cdot G_o \tag{2.4}$$

2.2.1 Reworking the MVD Modules

As of writing this thesis there is no established process to remove sensors off a built module. While there are ideas of careful mechanical removal or ablation of a sensor using laser, the presence of fully bonded FPC makes this task difficult. Additionally, mechanical removal of sensors or FPC cables runs the risk of damaging the coating of the carrier (see ch. 2.2.2). This would essentially ruin the module, as without the coating the sensor would short out through the carrier, as the material TPG has a high electrical conductivity. The adhesive could be an additional electric insulation but one has to take care to apply it uniformly. The success of reworking sensors on the carrier hinges entirely on the removal off the carrier without damaging the coating.

2.2.2 Baseline

The baseline (see fig. 2.1 top left) consists of a 380 μm thick plate of parylene-coated TPG with sensors on both sides (*1xDoublesided*). The coating ensures electric isolation of the back-biased Mimosis sensors. The sensors are glued onto the carrier using a radiation-hard glue (custom made RAL 247 [SD22]) and bonded to copper trace FPC cables. The FPC feeds the data to readout boards. The TDR [SD22] of the MVD describes a material budget of averaged over x and y (see fig. 2.2) around 0.4 % x/X_0 with a maximum of 0.53 % x/X_0 (see fig. 2.2). A computation done for this thesis arrived at a maximum of 0.43 % material budget, based on material property values.

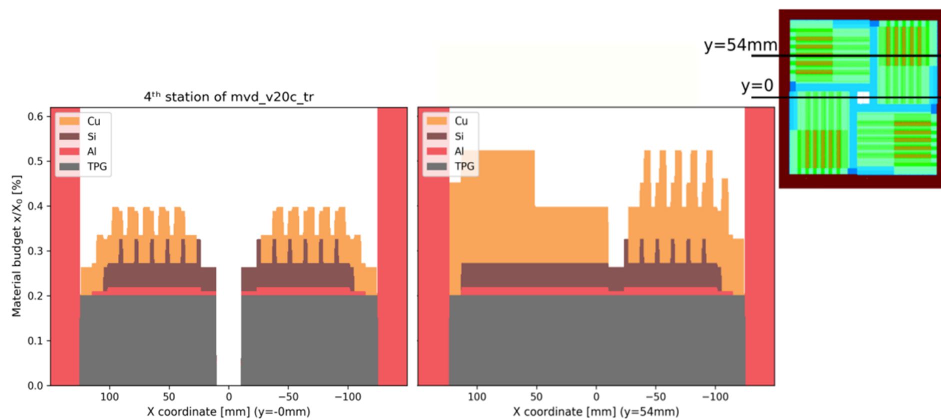

Figure 2.2 –

Material budget across x of geometry c of the MVD [SD22]. Top right image indicates where the cuts are on the layout. Cu: FPC, Si: sensors, Al: heatsink, TPG: carrier. The assembly flow works from top to bottom, left to right.

A TPG carrier 380 μm thickness is self-supporting. A jig provides sufficient security while handling the thinned MIMOSIS sensors for alignment and placement ([SD22] p.64/65 for concept). The assembly process begins with visual inspection and **Q**uality **A**ssessment(QA) of each component, then using a jig four sensors are aligned in a line and glued onto the frontside of the carrier. Next a FPC cable is glued onto the carrier and a visual inspection is done. The sensors are then bonded to the FPC cables. After bonding the FPC cables allow for testing if all sensors in a row survived the integration. Reworking a sensor would still be possible after bonding it to the FPC cables. The faulty sensor would be disconnected from the FPC cables

and removed off the carrier. Here, several issues may arise (see ch. 2.2.1). This process is repeated 6 more times for each line of sensors on the front and back. A final inspection of the assembly is done to confirm everything works as intended. The assembly flow is shown in fig. 2.3.

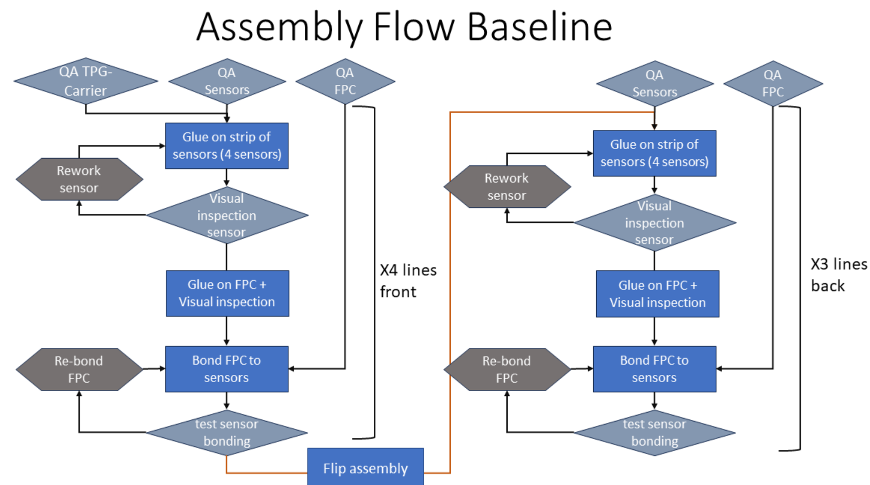

FIGURE 2.3 –

The assembly flow for baseline module assembly as envisioned in large blocks. Grey rhombic symbols denote QA steps, blue rectangles denote assembly steps. The hexagons denote reworking steps, if they are deemed possible.

This sets the baseline for all production discussion and can be qualitatively computed as eq. 2.5.

$$RTY_{baseline} = (I_1 \cdot B_1)^{16} \cdot G^8 M_1 \cdot (I_2 \cdot B_2)^{12} G^6 \tag{2.5}$$

Here it is assumed that the integration yield and bonding of the sensors on the backside is lower than on the front, $I_2 < I_1, B_2 < B_1$. The mechanical step M_1 denotes the flipping of the carrier to populate the backside. G denotes the gluing of the FPC cables to the module and is assumed to be equal on both sides for this discussion. As each cable connects to two sensors, it requires a total of 14 FPC cables. Each carrier option can be displayed as such an equation and compared.

2.2.3 Thinned Baseline

In comparison to the baseline, the thinned baseline concept (see fig. 2.1 top left) sacrifices thermal and mechanical performance to reduce the material budget by 0.07 % x/X_0 to 0.36 % x/X_0. It is based on a 250 µm thick TPG plate. It is a potential if the material budget needs to be reduced further, but it increases the difficulty in handling the carrier due to its thinness. The saving in material length would be $\frac{\sigma_{Tb}}{\sigma_{Bl}} = \sqrt{\frac{0.36}{0.43}} = 0,91$, so about a reduction of 10 % per geometry b/c used. It has a production yield and assembly flow qualitatively similar to baseline, as the only change is a thinning of the carrier. The thinning may increase the difficulty in handling the carrier, requiring more care than the baseline during assembly, but not impossible.

2.2.4 Ladders

As a concept, Ladders (see fig. 2.1 bottom left) separates the carrier into ladders, seven sensors on each ladder with four front/three back alternating (4xdoublesided). Each ladder is based on 380 µm thick TPG and boasts a similar material budget to baseline. Here the TPG is not thinned further so as to avoid mechanical instability during assembly. The process to construct a ladders based module starts with populating each strip with 4 sensors on the front and 3 sensors on the back. Each ladder is then visually inspected and mounted in the heatsink. This is repeated four times. Afterwards the FPC cables is bonded and glued perpendicular to the ladders. This is a point of issue as gluing and connecting the FPC cables across the ladders could prove challenging due to the requirement to bond across all ladders. If the heatsink is used as aligning jig, then the process may actually prove to be useful, as it would allow for easier removal of a set of sensors depending on the ease of un-gluing and re-gluing the FPC cables. The flow is shown in fig. 2.4.

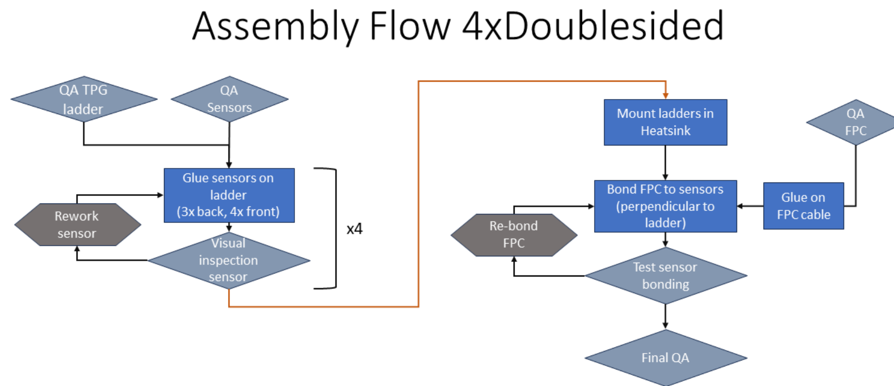

Figure 2.4 –

The assembly flow for a ladder based module assembly as envisioned in large blocks. Grey rhombic symbols denote QA steps, blue rectangles denote assembly steps. The hexagons denote reworking steps, if they are deemed possible.

2.2.5 2xOnesided TPG

The option of 2xOnesided TPG (see fig. 2.1 top right) separates the front- and backside of the carrier. As such, during the complex bonding process and sensor integration, no difficulty arises from sensors placed on the other side and reduces the number of sensors per sub assembly to 16 (front)/12 (back) respectively. For this option 150 µm thick TPG is to be used, to keep material budget in line with baseline. The material budget is 0.4 % x/X_0 if one assumes a uniform layer of glue with a thickness of ~ 40 µm to hold the front and back together. Here, the assembly flow is quite similar to baseline, but the large difference is that the front- and backside are assembled separately. Afterwards both sides are married inside the heatsink. Both sides are glued together with vacuum compatible glue. Here is a potential of saving even more material budget as it may be possible glue only a few spots between the front- and backside. The assembly flow is shown in fig. 2.5.

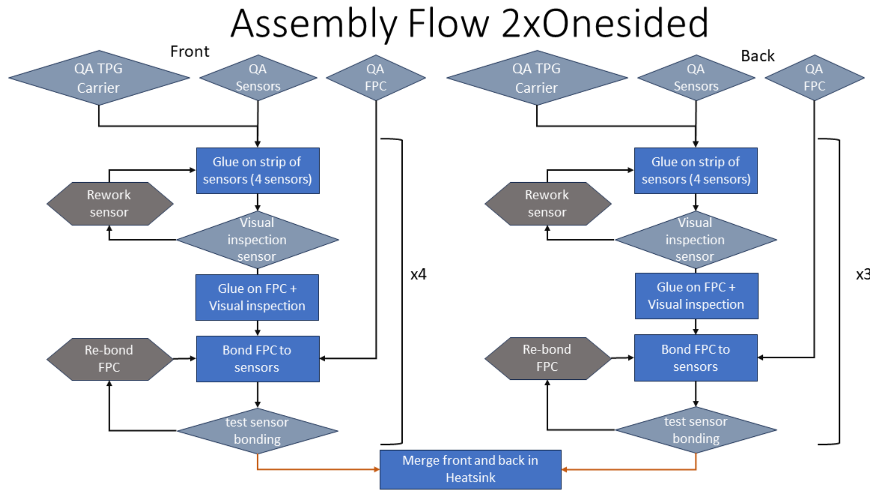

Figure 2.5 –
The assembly flow for a double sided module assembly as envisioned in large blocks. Grey rhombic symbols denote QA steps, blue rectangles denote assembly steps. The hexagons denote reworking steps, if they are deemed possible.

2.2.6 PGS And RVC Composite

A different approach to optimize the carrier, where the thermal requirements could be fulfilled by a thin PGS layer and the mechanical stability of the carrier is provided by RVC (see fig. 2.1 bottom right). RVC has a long radiation length and could reduce the material budget significantly. To produce a PGS/RVC composite, a layer of glue must be used between the two materials. As RVC is porous, an additional material like carbon fleece is needed to keep the glue from penetrating and running into the RVC [Mag21]. Afterwards, the process is similar to the integration of 2xOnesided TPG. Both carrier halves are populated with sensors with visual inspection after a row. FPC cables are glued on and bonded. Then QA is performed on each sensor. The steps are repeated for each row of sensors. The idea of RVC as a mechanical structure in detectors is currently being pursued by the ITS3 upgrade at ALICE [Mus19, M.A]. This option could reduce the material budget to $x/X_0 = 0.38\,\%$, which is less of a saving than anticipated. This calculation does not take the carbon fleece (an interface material) into account. The lower than expected reduction in material budget is due to the large amount of extra glue required (gluing PGS to RVC, marrying both sides). The envisioned production yield and assembly flow would be similar to "2xonesided TPG" as only the material changes.

2.2.7 Discussion of Production Yield

The main issue with the MVD in this discussion is that the yields of any step in the process of assembly for the MVD are not known. As such only assumptions can be made on the yield of each step and the rolling throughput yield of MVD. The following assumptions are postulated:

1 Per sensor row, a reduction of sensor integration yield is assumed for each sensor. Past the first one, due to butting of the sensors into each other and mechanical mistakes during alignment the yield of sensors integrated in one row past the first one is likely reduced.

2 For a carrier, whose front side is already bonded, the backside sensors incur a loss of yield during bonding the further away from the support (here it is assumed only the heatsink is used as structural support). This is due to the required pressure during the bonding process.

Using these assumptions, it is possible to produce equations that should allow discussion on the merits of each option. For this, 2.5 is expanded:

$$RTY_{Baseline} = (I_1 \cdot I_2^3)^4 \cdot B_1^{16} \cdot M \cdot (I_1 \cdot I_2^3)^3 \cdot B_1^6 \cdot \prod_{i=2}^{4} \prod_{j=2}^{3} (B_{i,j} - (C_2 \cdot (i-1)) - (C_2 \cdot (j-1))) \cdot G^{14} \quad (2.6)$$

Here, I_1 is the base yield of gluing a sensor independently. Assumption 1 then postulates that each subsequent sensor in a row follows $I_2 = I_1 - C_1$ where a small reduction in yield (constant C_1) is subtracted off the yield. The bonding B_1 of the front sensors is assumed to be independent for each bond as the module would be lying on a support structure. The risk yield of turning over the assembly in the jig is noted as M. Following this, using assumption 1 the steps for sensor integration are calculated again. Assumption 2 is then expressed in a product where each sensor that is not next to the heatsink (the first row and each sensor in the first column) incurs a small increasing loss the further away from the heatsink it is, denoted with $C_2 \cdot i, j$. This can be visualized if one imagines the sensors as a grid with i,j as the rows and columns.

Similar equations can be assumed for the other potential construction options:

$$RTY_{Ladders} = (I_1^7)^4 \cdot \prod_{i=1}^{4} M_i \cdot (\prod_{i=1}^{4} (B_1 - (C_3 \cdot (i-1))))^4 \cdot (\prod_{i=1}^{3} (B_1 - (C_3 \cdot (i-1))))^4 \cdot G_L^{14} \quad (2.7)$$

$$RTY_{2xonesided} = (I_1 \cdot I_2^3)^4 \cdot B_1^{16} \cdot (I_1 \cdot I_2^3)^3 \cdot B_1^{12} \cdot M_D \cdot G^{14} \quad (2.8)$$

For ladders the yield loss is assumed to be $C_3 > C_{1,2}, G_L > G$, as gluing of the FPC cables and bonding of the sensors happens perpendicular to the ladders and incurs a potentially larger loss due to it. This happens due to the issue of applying pressure for bonding on an object that is only clamped on one end. In the case of the double sided option the advantage is easy to spot as the complex loss of bonding yield from baseline is removed. A high mechanical yield M_D is still required for it to stay competitive against baseline which includes integrating the ladders into the heatsink as well as the alignment of each ladder. From these assumptions, the 2xOnesided option provides potential to reduce the complexity and difficulty of the production, possibly increasing yield. Until the final process is decided, these equations only give a rough outlook at the potential differences.
For further discussion one can assume the yield of I or B to be equal to one. If I=1, then the equations change to:

$$RTY_{Baseline} = B_1^{16} \cdot M \cdot B_1^6 \cdot \prod_{i=2}^{4} \prod_{j=2}^{3} (B_{i,j} - (C_2 \cdot (i-1)) - (C_2 \cdot (j-1))) \cdot G^{14} \tag{2.9}$$

$$RTY_{Ladders} = \prod_{i=1}^{4} M_i \cdot (\prod_{i=1}^{4} (B_1 - (C_3 \cdot (i-1))))^4 \cdot (\prod_{i=1}^{3} (B_1 - (C_3 \cdot (i-1))))^4 \cdot G_L^{14} \tag{2.10}$$

$$RTY_{2xonesided} = B_1^{32} \cdot M_D \cdot G^{14} \tag{2.11}$$

In this case, $\mathrm{RTY}_{\mathrm{2xonesided}}$ has the highest yield due to the equation depending only on B and $\mathrm{M_D}$. No constants are subtracted off B_1 and as such it reaches the highest comparative yield. The next highest yield is baseline as it contains only one mechanical factor M in comparison to ladders' four. Additionally as $C_3 > C_2$, the yield of ladders will likely be lower than baseline.

Conversely, if B is equal to one:

$$RTY_{Baseline} = (I_1 \cdot I_2^3)^7 \cdot M \cdot G^{14} \tag{2.12}$$

$$RTY_{Ladders} = (I_1^7)^4 \cdot \prod_{i=1}^{4} M_i \cdot G_L^{14} \tag{2.13}$$

$$RTY_{2xonesided} = (I_1 \cdot I_2^3)^7 \cdot M_D \cdot G^{14} \tag{2.14}$$

The discussion changes as the yield difference between baseline and 2xonesided reduces to a difference in M. Depending on $M_D \lessgtr M$ 2xonesided wins out in yield estimation. The highest

yield could be achieved by ladders as $I_2 < I_1$, if G_L is compensated for by a substantial increase in yield for the mechanical steps. If the change to only I_1 can equal out the additional Ms, then ladders would win out in yield if the bonding is always successful.

For a visual representation the rolling throughput yield can be expressed using a set of assumed yields for each step. In this case, the bonding yield is assumed to be perfect based on the ease of rework, as long as the carrier is not damaged (B=1). Next, I_1 is held variable to cover a range of possible outcomes depending on the most important set of steps, integrating the sensor. It is assumed that each sensor past the first one in a strip reduces the yield by C_1=2% with an additional 2% reduction for the integration on the backside if the front has already been populated. The discussion focuses on the baseline and 2xOnesided with the mechanical yield being M=99% and M_D=99.8% assuming the merging of a carrier is easier than flipping it without damage. The integration step G for gluing the FPC cables is assumed with a yield of 99.5%.

Figure 2.6 shows that the 2xOnesided option has a higher production yield, able to reach a RTY>50% near the upper 99%-tile for sensor integration yield. Conversely due to the loss of yield on the backside, baseline loses more potential yield, only able to reach the upper 40%-tile. This highlights the critical need for the ability to rework components. Reworking can push the yield of a step higher up, allowing the rolling throughput yield to be as high as possible. The dependence on a very high integration yield for the rolling throughput yield crystallizes into the following conclusions for the production process:

1 The ability to rework components can increase the yield per step (see eq. 2.3) and should be further followed up on where and how it can be performed.

2 QA of individual parts and steps is important to catch damaged components early on.

3 The team performing the actions should be comprised of a small group of "experts", people who can understand the processes and are trained on each step performed.

4 High quality tools can increase the yield by increasing accuracy and reducing damage from handling.

These conclusions all increase production yield per step, which will help with lifting the overall rolling throughput yield. Of note here is that RTY is mainly used in large volume manufacture

and as such should be taken more as a guide line for low volume production as seen in research. It helps with highlighting critical issues within a process but is a vague value more useful in theoretical discussions. In addition here the increase in yield over time is not taken into account as people get more accustomed to the processes and improve upon them.

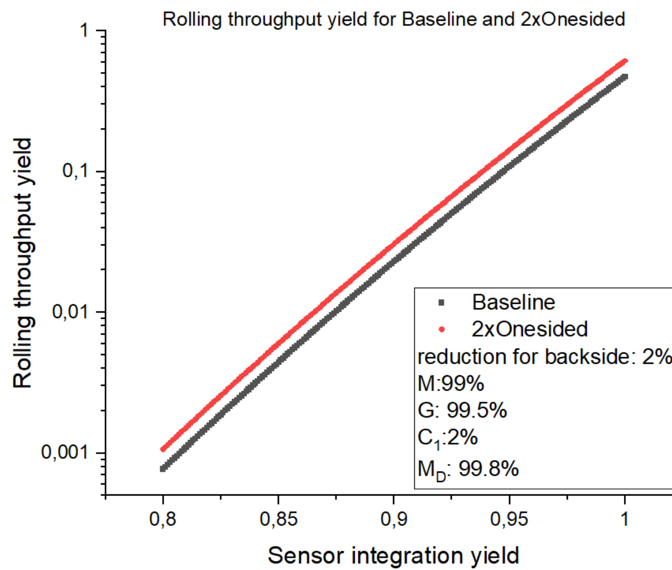

Figure 2.6 –

The rolling throughput yield of Baseline and 2xOnesided based on assumed yields. Assumed were B=1, C_1=0.02, additional loss of 0.02 for the backside, M=0.99, M_D=0.998, G=0.995. RTY>0.5 only happens for 2xOnesided near 0.995 for the sensor integration yield I, with Baseline only reaching about 0.44. This highlights the need for achieving very high yields per step, for which the ability to rework components is critical.

2.3 Material discussion

A figure of merit is used to select materials based on properties that are combined to show which material is suitable. Examples could be a figure of merit for thermal and electrical properties based on temperature. For the MVD the figure of merit is comprised of the thermal conductivity $\lambda$and radiation length X_0 (see fig. 2.7.

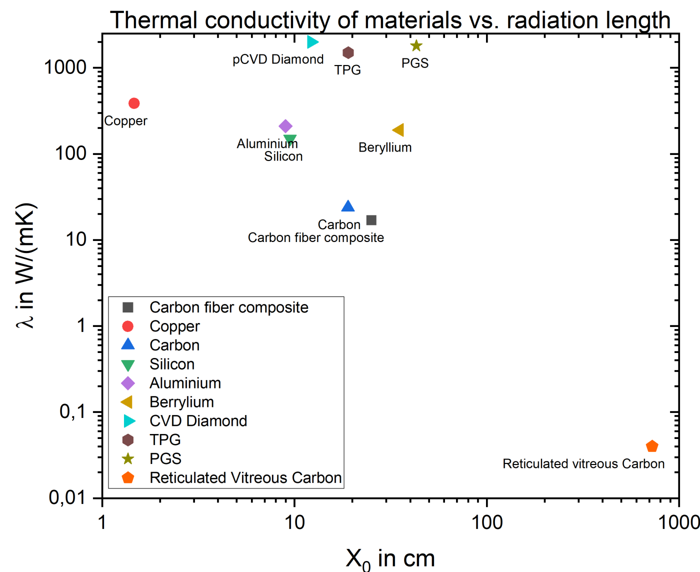

FIGURE 2.7 –

The thermal figure of merit for different materials. The chosen properties are thermal conductivity λ in $\frac{W}{m \cdot K}$ versus the radiation length X_0 in cm. Each axis is shown in log_{10}.

The graph in fig. 2.7 shows that carbon based high performance materials are clear favorites. Special note is to be given to TPG, PGS and pCVD diamond, being far and away from other options that could be chosen. Of note for PGS is that it has a very high thermal conductivity, but essentially no mechanical strength. Of additional interest is reticulated vitreous carbon (RVC). It has one of the largest radiation lengths measurable (over 700 cm) while being mechanically rigid but brittle. A compound material of PGS and RVC could therefore reduce the material budget significantly. Additionally the coefficient of thermal expansion for the carbon materials are all very close to each other (between 0.9 to 2 1/K). The CTE for silicon is around 3 1/K. The glues chosen for the MVD have CTE of 50-60 1/K.

2.3.1 Thermal Pyrolytic Graphite

Thermal **P**yrolytic **G**raphite (TPG), see fig.2.9 a,is produced by heating hydrocarbon gas until it decomposes, utilizing a chemical vapour deposition (CVD) process to grow layers of the material. This produces a highly anisotropic material with excellent thermal conductivity in the xy-plane (1500-1700 $\frac{W}{m \cdot K}$), but low conductivity in the z direction (less than 20 $\frac{W}{m \cdot K}$) [Mom]. The material is essentially highly ordered graphite with mechanical properties like graphite. It can be cut using a laser cutter as well as gentle, repeated cuts with a sharp blade (the produced particles from cutting can be toxic when inhaled). It is also easy to deform, as such requiring care when handling. The radiation length of TPG is 19.03 cm X_0. It's Youngs Modulus is 150 GPa in the xy-plane. The CTE is $1 \cdot 10^{-6}$ 1/K.

2.3.2 Pyrolitic Graphite Sheets

Pyrolitic **G**raphite **S**heets (PGS), see fig.2.9 b, are created by the process of sintering a layer of polymer until it carbonizes, then sintering it again to align the "hexagonal carbon ring array graphitic structure" [Pan]. This generates a thin layer of thermally conductive graphite with highly anisotropic properties. As specified in [Pan], the thickness of the material defines the thermal conductivity (see fig. 2.8). It is too thin to mechanically support itself or anything adhered to it, as such it is only useful for its thermal properties.

Additionally, adhering anything to it with glue is a difficult process as the material is nearly non-stick. As for its radiation length, the manufacturer does not specify. However, as it is essentially graphite, it can be inferred that the radiation length should be that of pure carbon of around 18.99 cm X_0. It's Youngs Modulus is around 20 GPa and the CTE is around $0.5 - 1.0 \cdot 10^{-6}$ 1/K.

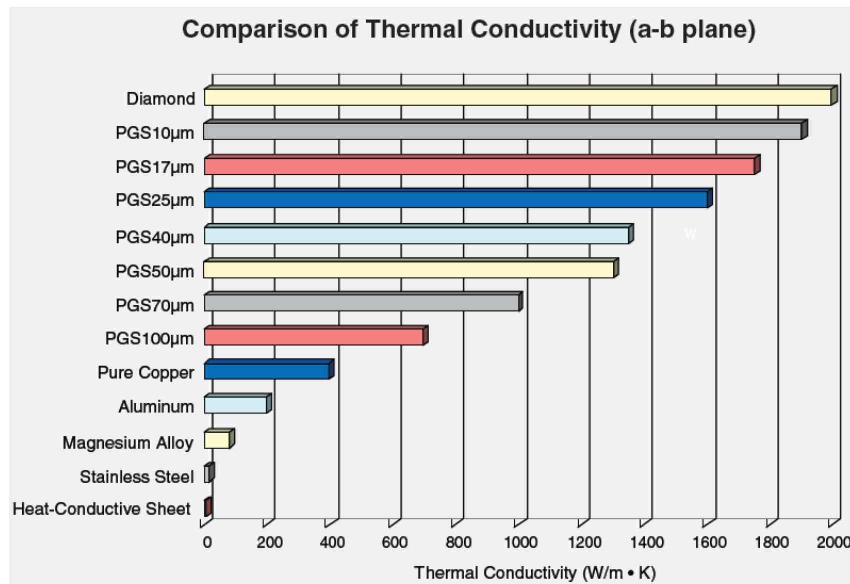

Figure 2.8 –

A comparison table for thermal conductivity (in $\frac{W}{m \cdot K}$) of the different thicknesses of PGS the manufacturer can provide and compared to other materials such as copper and aluminium [Pan]. This shows the clear superiority of graphite based thermal conductors in the xy-plane as well as the thickness dependence of λ for PGS.

2.3.3 Reticulated Vitreous Carbon

Reticulated **V**itreous **C**arbon (RVC), see fig.2.9 c, is created by heating a carbon based foam under a nonreacting atmosphere and vitrifying it. This creates a lightweight, porous material with high stiffness strength and high surface area. Depending on the foam used in the initial creation, a varying density and pores per inch (ppi) can be achieved. Its bulk thermal conductivity is ~0.03-0.05 $\frac{W}{m \cdot K}$ [ERG].
The most relevant property for this thesis is its extremely low radiation length (x/X_0=0.02 % at 2 mm thickness of material, 728.95 cm X_0) and a CTE of $2 \cdot 10^{-6}$ 1/K. As a sidenote RVC foam also has a very large internal surface area, making it a highly efficient heat exchanger if gas is pumped through the foam. As MVD operates in a vacuum, one unfortunately cannot take advantage of this property.

All material features are listed in table 2.2 for ease of comparison.

Material	λ in $\frac{W}{m \cdot K}$	X_0 in cm	E in GPa	CTE in 1/K
TPG	1500(20)	19.03	150	$1 \cdot 10^{-6}$
PGS	1350(20)	19.03	20	$0.5 - 1 \cdot 10^{-6}$
RVC	~0.03-0.05	728.95	0.5	$2 \cdot 10^{-6}$

Table 2.2 –
The table lists the material properties of the carrier materials for ease of comparison. Bracketed values denote anisotropic materials and the value in z direction.

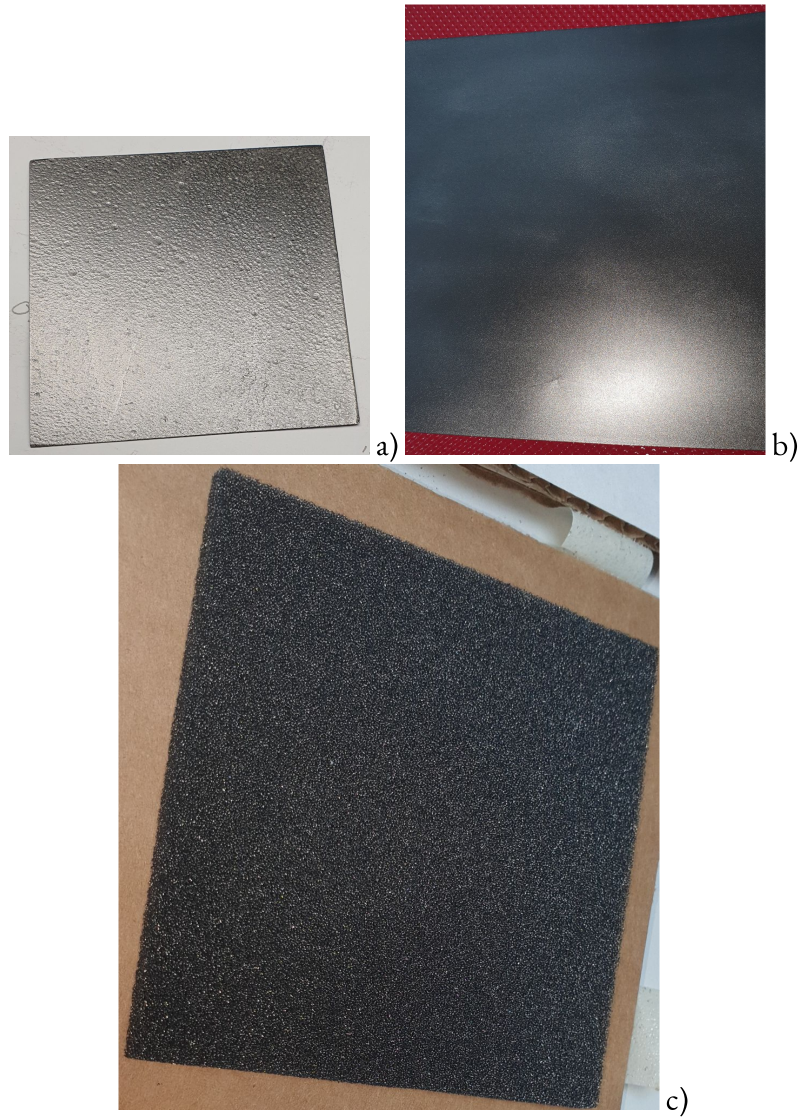

Figure 2.9 –

The different materials used in this thesis shown.

a) TPG sheet (380 µm), b) PGS foil (40 µm), c) RVC (200PPI, 2 mm).

Thermal Testing and Validation 3

As part of this thesis the thermal properties of TPG and PGS are verified. For this, copper is used as a reference material due to its well known thermal properties. Then the thermal conductivity of TPG and the PGS/RVC compound are measured. Using the results thermal simulations are tuned to predict the behaviour of the carrier design options. Afterwards the simulations are verified using carrier sized pieces of TPG and PGS/RVC compound to compare. To facilitate this, a vacuum chamber is required to test in to MVD relevant environments. The samples are to be heated using simple heating pads while the experimental results are measured using sensors on the sample and inside the test chamber. Additionally an **I**nfra**r**ed (IR) camera is used for comparison.

3.1 Test Setup "UFO"

The UFO is a vacuum test chamber setup at the Goethe university Frankfurt. It is used to test various parts of the MVD design, such as the cooling loop, the carrier material and heat sink designs. It features feedthroughs for (currently) Novec-649 based liquid cooling, several ports for data and electric cable management. The setup can achieve a vacuum of up to 10^{-7} mbar. Additionally it also features a top mounted infrared window with an IR camera mounted to view inside the chamber (fig. 3.1 top red box).

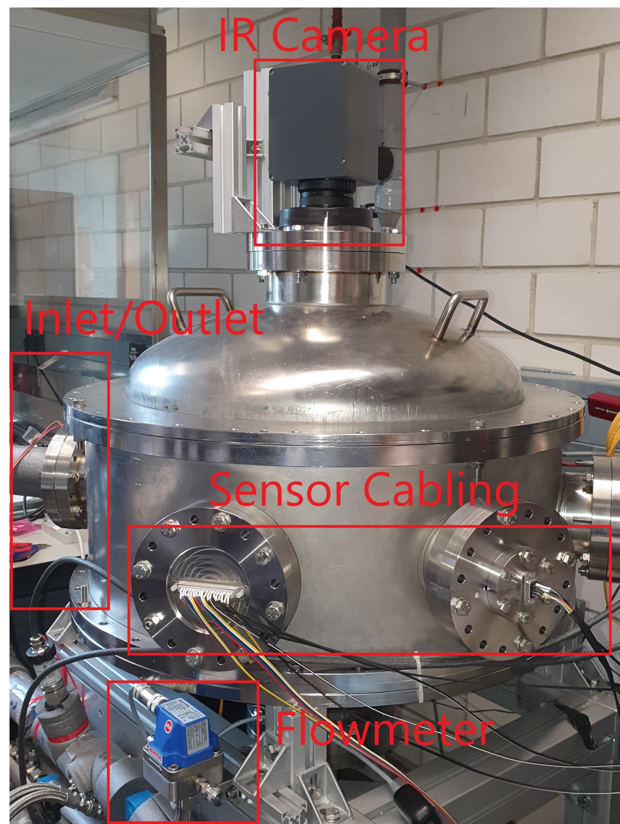

Figure 3.1 –

A photo of the UFO experimental setup from outside. It shows the placement of Inlet/Outlet feedthrough, feedthrough for cable connections, the flowmeter for coolant and the IR camera. The actual inlet/outlet are not visible.

3.1.1 Cooling Loop

The operation temperature of UFO extends from −35 °C to +25 °C and is enabled by the use of Novec-649 [3M09], a cooling fluid featuring a low viscosity at the stated temperature range, enabling mono phase cooling. Novec is aggressive towards plastics and rubbers with plasticizers. Due to this, stainless steel piping with standard SWAGELOK compression fittings are used. For threaded connections Loctite-511 is utilized. To pump and cool the Novec-649, a PRESTO A40 cooling unit from JULABO is used. This is done due to the highly evaporative nature of Novec-649. Additionally it does not mix with water. These properties require a closed loop for sustained operation. The simplified diagram of the cooling loop used is depicted in figure 3.2.

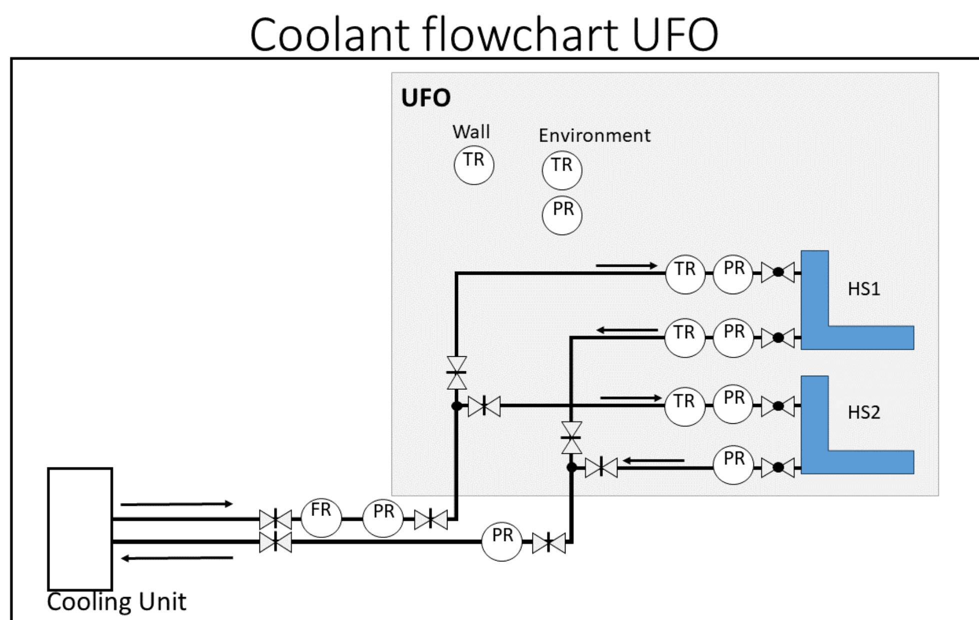

FIGURE 3.2 –
Flowchart of the cooling loop of UFO, showing the valves and recording equipment was used in the system. HS1,2: heatsinks and carriers. TR: temperature recorder, PR: pressure recorder, FR: flow recorder. The grey box denotes the inside of the UFO.

Regarding details of the cooling loop, please refer to the Bachelor thesis of Franz Matejcek [Mat22].

3.1.2 Pt100 Sensors

Pt100 sensors are used to measure temperature [Nex]. By using two dedicated boards developed by J. Michel, P. Klaus and M. Wiebusch, a total of 16 sensors can be read out. This is done by applying a small current and measuring the relative voltage drop over a 100 Ω resistor on the board. The signal is then digitized and processed on a computer. Two sensors are wetted sensors, placed inside the cooling loop right before the inlet and outlet of the heat sink. The other 14 sensors are distributed in the setup to gain a comprehensive picture of the thermal distribution. Four sensors are reserved for the heat sink, one sensor each for the UFO ambient and wall temperature as well as eight sensors for the DUT itself. “Super glue” ($\lambda \sim 1.2 \frac{\mathrm{W}}{\mathrm{m \cdot K}}$) is used to attach them to DUTs.

In industry literature (see [Nex]) a tolerance is given for a sensors uncertainty. It is taken as the **systematic error** of the sensors. Per the class DIN 1/3 B given for the sensors used, the tolerance/**systematic error** lies at 0.1 K [Nex] at 0 °C with a maximum of 0.2 °C at ±60 °C. As measurements are taken on a large span of temperatures, a constant 0.2 °C is used. A further limiting factor of the setup is that temperatures past 65 °Ccannot be measureddue to limitations of the temperature readout system. The **statistical error** was evaluated using a large number of measurement points at two sensors at -30 °C coolant temperature. The RMSE-error was then computed in figure 3.3 and comes out at around 0.05 °C.

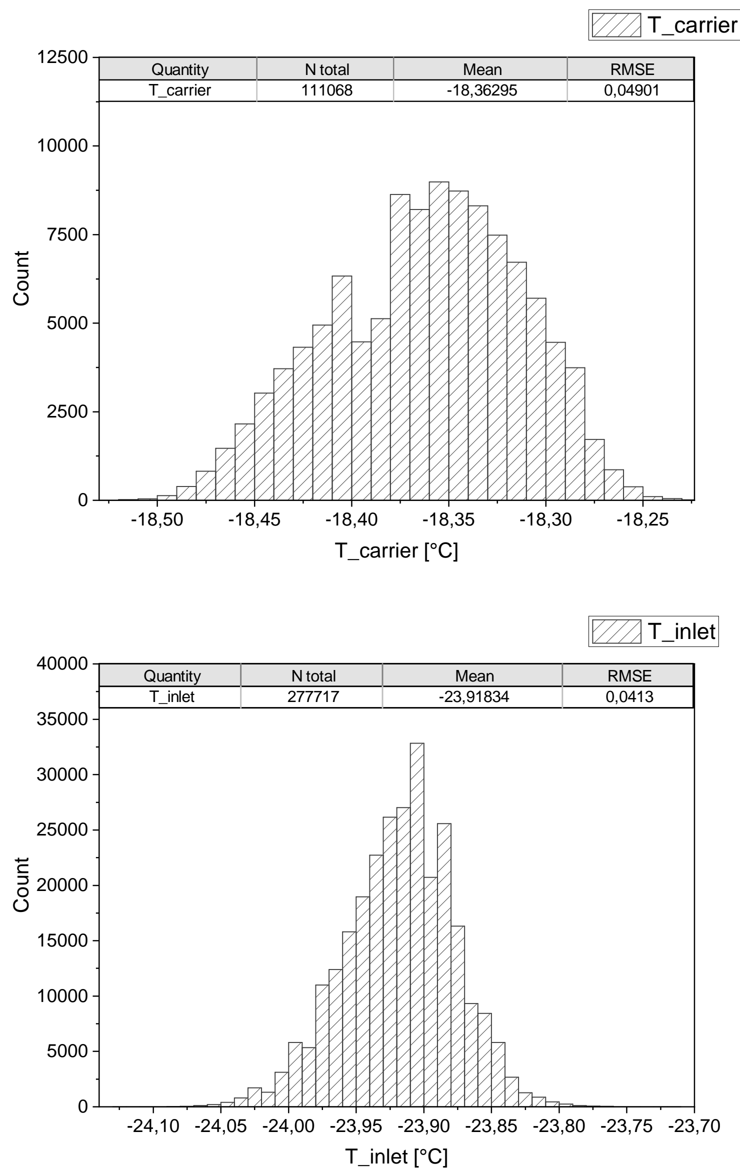

Figure 3.3 –

Temperature readout distribution of a single sensor [F.M] over a long period of time. Using RSME error evaluation the statistical error for the PT100 sensors is extratcted. Top: sensor located on the TPG carrier. Bottom: sensor located at the cooling loop inlet for the heatsink.

3.1.3 IR Camera

The infrared (IR) camera "Variocam head HiRes 640" by Jenoptik [Jen] and Infratec [Inf] has been mounted ontop of the UFO's lid (see fig. 3.1 red box at the top). The camera works based on microbolometers in a focal plane array. A microbolometer works by employing an IR absorbing material and a thermometer to measure changes in temperature [BSJL09] (see fig. 3.4).

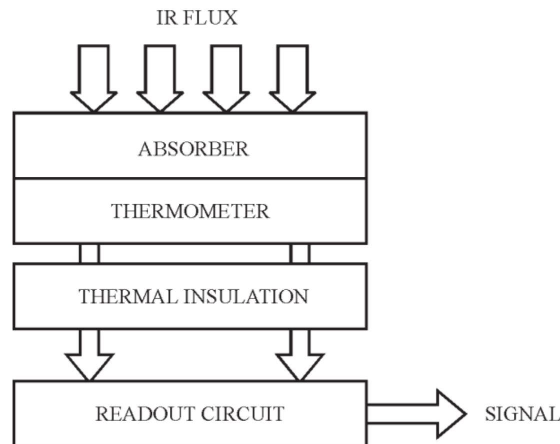

Figure 3.4 –
A simple schematic of how a bolometer works [BSJL09]. To achieve a high sensitivity the ROIC are thermally isolated from the bolometers.

The change in temperature in the thermometer material translates to a change in electrical resistance. A readout circuit then makes the measured temperature available to further software. A big advantage of bolometers is that they require no extra cooling to work, only the excess heat has to be transferred off with the help of a fan.

To enable the camera view into the chamber, an IR transparent germanium-based vacuum window is integrated. This allows for independent measurements of the absolute temperature after initial calibration based on the Pt100 sensors. The camera achieves measurement rates of 60 Hz and a global temperature variance of ±0.4 K. A pixel by pixel inaccuracy of ±0.05 K is possible as per manufacturer [Inf15, sup22]. The global temperature variance is a systematic value that shifts the entire measurement in one direction. As this thesis is concerned with a temperature difference ΔT, the global variance cancels out after calculating the difference. A software package called "Irbis 3Plus" by Infratec is used to monitor and display the cameras

data as a live feed or a recording, which can be analysed and exported. Furthermore the package allows for marking areas of interest on the measured object to read out numerical data of the temperature at that spot. The "Object through path and window" setting (see fig. 3.5) was chosen as the carriers are viewed through an IR window and a large distance.

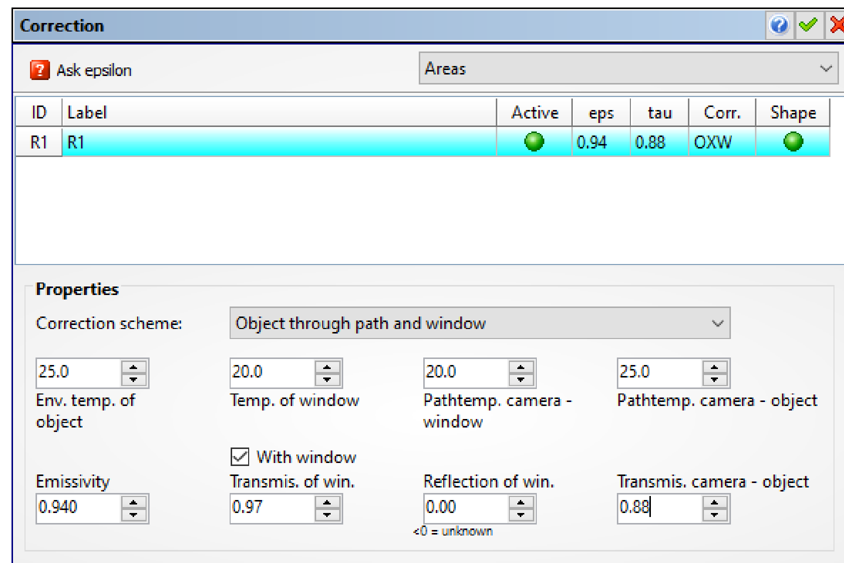

Figure 3.5 –

The corrections used in the IR camera. The settings were held static besides "Transmission Camera-Object". This value was tweaked on a measuring run basis to calibrate the camera onto the sensors.

3.1.4 Other Sensors

To monitor the pressures and flows inside the setup, pirani gauges are used for the vacuum chamber while wetted pressure transducers and a flowmeter provide information about the coolant loop. This is used to monitor the setup during measurements.

3.1.5 Kapton Heater

The heating elements for the experiments are kapton based heating pads with a copper trace inlay and an adhesive backside. Using a power supply the induced heating power can be adjusted within a range of ±0.01 W. The used sizes of the pads vary between 1x1 in^2, 2x2 in^2 and 4x4 in^2, depending on the experiment. The smaller pads have a lower maximum voltage threshold that can be applied. This results in a safe maximum of 5.5 W heating power for the smaller pads used. The larger pads have a much higher maximum voltage and can reach heating powers in excess of 20 W.

3.1.6 Thermal Conductivity

Thermal conductivity is the property of matter to transfer thermal energy or "heat" through itself. The defining equation for thermal conductivity is a scalar for the heat flux $\dot{Q}$ (see eq. 3.1), made up of thermal conductivity λ in tensor form and the temperature gradient ∇T.

$$\dot{\vec{Q}} = -\lambda \vec{\nabla} T \tag{3.1}$$

This can be simplified into one dimension and given as an equation calculating the thermal conductivity. For the one dimensional case, consider:
If one assumes a wall with thickness l between two temperature reservoirs with temperatures $T_1 < T_2, \Delta T = T_2 - T_1$ and refers to a given area A comprised of the width w and height h of that wall, one finds a heatflow $\dot{Q}$ between the reservoirs through the wall piece. Equation (3.2) shows how thermal conductivity in one dimension is computed.

$$\lambda = \frac{\dot{Q} \cdot l}{A \cdot \Delta T} = \frac{\dot{Q} \cdot l}{w \cdot h \cdot \Delta T} \tag{3.2}$$

The thermal conductivity λ has the resulting form of $\frac{\mathrm{W}}{\mathrm{m \cdot K}}$.

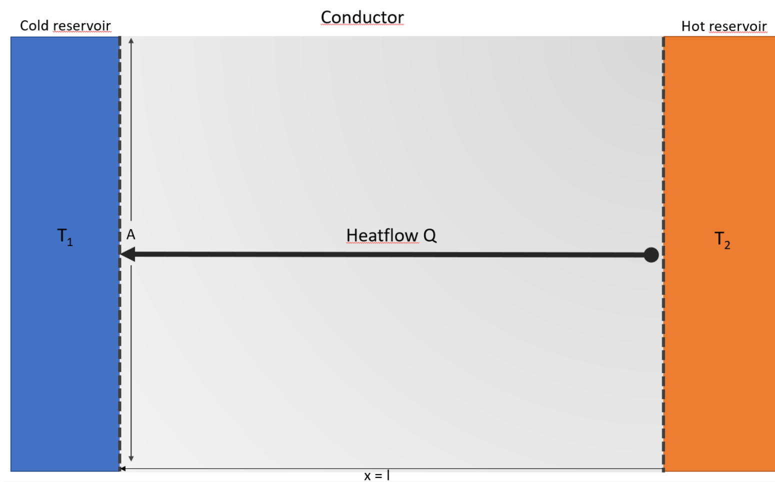

Figure 3.6 –

A graphic showing how eq. 3.2 works, depicting the Heatflow Q through the conducting material (Conductor) with area of contact A and thickness x = l.

3.1.7 Calculating Temperature Difference of Baseline

A calculation for the temperature difference of a MVD baseline module is done. It is based on a parylene coated sheet of TPG with 28 sensors (station geometry c). The TPG carrier is clamped into the aluminium heatsink. The thermal interfaces between materials are approximated to zero due to their thickness approaching zero, while having a large contact area. A power density of $100\frac{\text{mW}}{\text{cm}^2}$ is assumed for this calculation. The thermal conductivities for each step are $\lambda_{sensor}=150\frac{\text{W}}{\text{m}\cdot\text{K}}$, $\lambda_{glue}=1.2\frac{\text{W}}{\text{m}\cdot\text{K}}$, $\lambda_{parylene}=0.1\frac{\text{W}}{\text{m}\cdot\text{K}}$, $\lambda_{carrier,x\text{-}y}=1500\frac{\text{W}}{\text{m}\cdot\text{K}}$ and for the contact between the carrier and heatsink, the z-direction conductivity of TPG is used, $\lambda_{carrier,z}=20\frac{\text{W}}{\text{m}\cdot\text{K}}$. For the steps from sensor to carrier the equation 3.2 is changed into $\Delta T = \frac{\dot{Q}\cdot l}{A\cdot\lambda}$, with $\dot{Q}/A$ taken as the power density. As such only the thickness and thermal conductivity of each material is necessary until the carrier is reached. The macroscopic contact between carrier to heatsink has an area of 36 cm^2. Due to the microscopic surface details of TPG, it is assumed only 1% of it actually makes contact. The surface structures of the TPG are up to 55 µm high. With this data a graph showing the accumulated temperature difference and point to point difference can be created as seen in fig. 3.7.

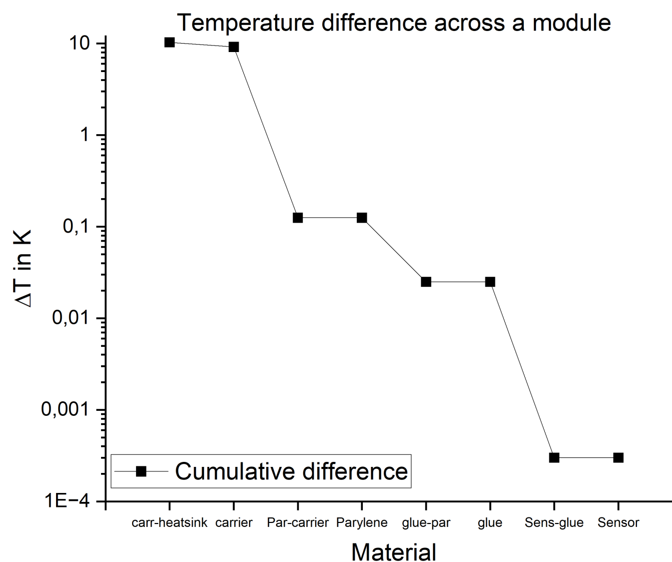

Figure 3.7 –

The different thermal steps of a module up to the heatsink as calculated cumulative steps.

3.1.8 Error Discussion

Based on equation 3.2 the errors identified for this experimental setup are discussed. It can be split into three parts: the heat entry $\dot{Q}$, the physical dimensions $\frac{l}{A} = \frac{l}{w \cdot h}$, with l being length, w being width and h being the height of the sample and the temperature component $\Delta T = T_2 - T_1$ being the thermal difference measured between two points along the path from hot to cold.

The heat entry $\dot{Q}$ is introduced by the kapton heaters. Here the heaters themselves could introduce uneven heating due to manufacturing defects in the copper wire inside the pad. Additionally the glue contact between the heater and the sample could be bad, reducing the available area for heat transfer. A small amount of the heating power is also transferred off through the cables of the heating pad themselves. The heating pads are powered by a power supply.

The physical dimensions have an error attached from measuring the size of test objects.

Further mechanical considerations are centered around the construction and use of the experimental setup. The samples are to be clamped with a constant and comparable torque of 0.4 Nm on the screws. Given a high enough torque this should minimize the contact temperature difference between the sample and the heat sink.

The amount of glue is minimized under each sensors. The layer of adhesive between the Pt100 sensor and the carrier is estimated to be in the range of 10 to 30 μm thickness. The heat transfer through the cables connecting the sensors is assumed to be negligible. Faulty sensors can be found easily by comparing to other sensors at $P_{heating}$=0 W.

The behaviour of the system is also of importance. After a change in $P_{heating}$, the system has to stabilize. The relaxation can be described as an inverse exponential function $T_{equalized} = T' \cdot e^{-\frac{t}{\tau}} + T_0$. τ denotes the relaxation time after which the temperature has reached 1/e of the final temperature. A wait time of 4-5 times τ is chosen. This was tested using a 250 µm thick carrier at 0 °C coolant temperature. The heat entry was 20 W (see fig. 3.8). This shows that a relaxation time of around 100-120 seconds is sufficient to reach a stable state.

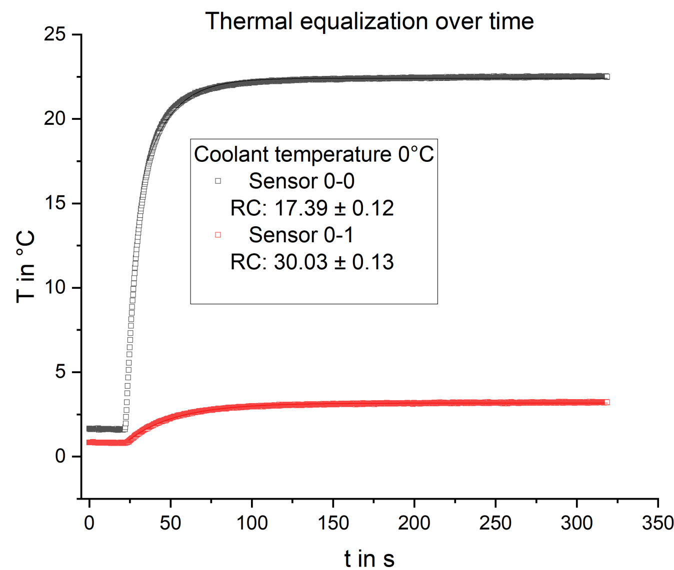

FIGURE 3.8 –

The thermal equalization at sensor position zero and one are displayed. They follow an inverse exponential function and flatten out after a given time 4-5 times the factor τ.

An additional factor could be a difference between the front- and backside of a sample. To discuss this, data from a 380 µm thick TPG carrier measurement is used. The thermal difference between a sensor atop the carrier and underneath the carrier is displayed against the heating power for each measurement cycle at different coolant temperatures. The temperature difference is shown in figure 3.9 and shows that no significant temperature difference exists between the top and bottom. Furthermore, this implies that the TPG material can be treated as a homogeneous two-dimensional material if thin enough as the thermal difference between top and bottom is minimal.

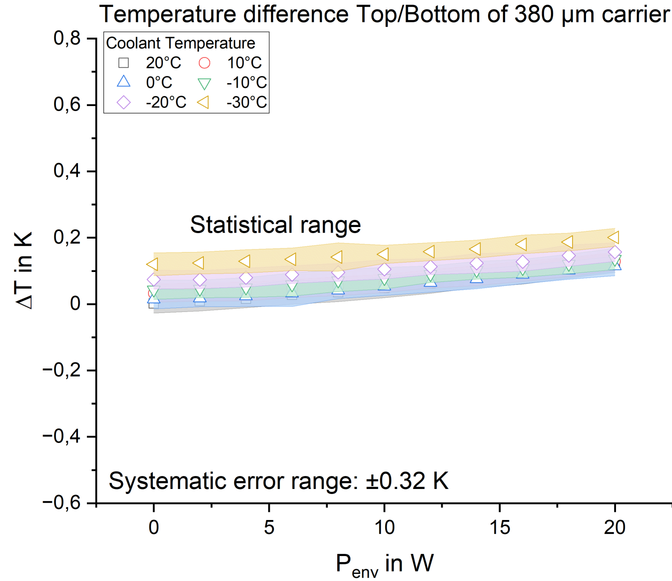

Figure 3.9 –
The thermal difference between the top and bottom of a 380 µm TPG carrier. Both sensors are placed ontop of each other and glued on with superglue. The ΔT is minimal, following within the statistical error. The systematic error is much larger and appended in the legend.

Another correction is from thermal input of the environment. At $T_{setup} < T_Z$, a thermal entry into the object is present from the surrounding chamber walls. Conversely, at temperatures above room temperature, the sample radiates more energy off than it gains. To calculate the input from the environment, a modified Stefan-Boltzmann law from [Thi09] is used:

$$\dot{Q} = \frac{\sigma \cdot (T_{wall}^4 - T_{sample}^4)}{\frac{1-\epsilon_{wall}}{A_{wall} \cdot \epsilon_{wall}} + \frac{1-\epsilon_{sample}}{A_{sample} \cdot \epsilon_{sample}} + \frac{1}{A_{sample}}} \tag{3.3}$$

The variables and constants in table 3.1 are used to calculate the different power entries for temperature of the sample (See also [Mat22]).

Using eq. 3.3, a set of curves that describe the additional heat entry of a given sample size are calculated, shown in fig. 3.10. For the measurements in fig. 3.10, the T_{Wall} and T_{Sample} is read out per data point. It is then put into eq. 3.3. Reference calculations at T_{env}=15/25 °C were done to provide comparison graphs. Two points at $T_{coolant}$=-20 and -10 °C lie at the upper band of calculations for 25 °C. This happened due to the room's environmental control being

Variable	value
σ	$5.67 \cdot 10^{-8} \frac{\mathrm{W}}{\mathrm{m^2K^4}}$
R	0.25 m
A_{Wall}	$0.4\,\mathrm{m}^2$
ϵ_{Wall}	0.05
A_{Sample}	a) 0.002- b) 0.018 m^2
ϵ_{Sample}	0.94

Table 3.1 –
Variables and constants used in the calculation of heat entry from the environment onto the sample. The area of the sample is dependant on which sample size is used, a) being for a thermal conductivity test strip and b) for a station c size test.

changed during the measurement cycle. All other points lie more towards T_{env}=15 °C as this was the set temperature on the thermostat. This extra power can be added to P_{heater} to arrive at P_{Total}. For a full quadrant of station c, with 28 sensors, produces 11.72 W total at 100 $\frac{\mathrm{mW}}{\mathrm{cm}^2}$. This is calculated based on the active pixel area of each sensor (31.15 × 17.25 mm^2) multiplied by the number of sensors (28) and then multiplied by the power density (100 $\frac{\mathrm{mW}}{\mathrm{cm}^2}$). At the lowest $T_{coolant}$, P_{env} from UFO corresponds to about 1.75-2.25 W but this is spread equally over the entire surface area. As such, a power density of about 8-12 $\frac{\mathrm{mW}}{\mathrm{cm}^2}$ is achieved. Its impact will be discussed further in ch. 3.5.1. The final power values in the full MVD environment will differ significantly.

The camera has to be calibrated due to the IR window transmissivity of t=0.97, the distance and the emissivity (ϵ=0.94) of the sample. For this the value of the transmission between the camera and object is tweaked until the point measurements of the camera agree with the sensors within acceptable tolerance (<0.5 K), as seen in fig. 3.5.

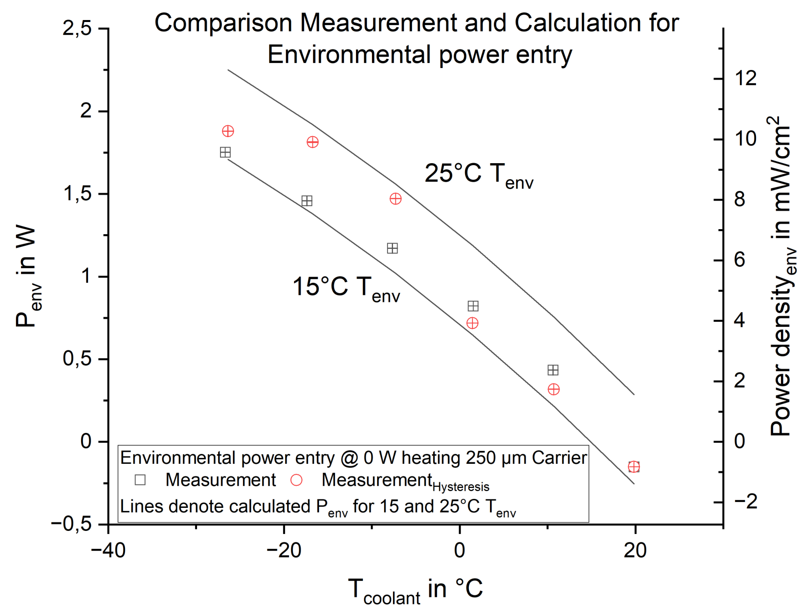

Figure 3.10 –

Graphical representation for eq. 3.3 w.r.t. varied environment temperature and sample temperature. The experimental data was taken using the thin carrier as described in ch. 3.5. For it the power entry was set to 0 W. P_{env} was measured from -30°C to +20°C and back down again in 10°C steps. The calculations were based off the carriers proportions and range of measured environmental temperatures.Significant changes of P_{env} at -10 and -20°C for hysteresis stem from a change of environmental temperature.

3.2 Error calculations

For general error calculations, one has to consider the equations for the measurements, the ΔT and the thermal conductivity.

For the measurements, one combines the statistical and systematic error. The error of ΔT and thermal conductivity λ is calculated as seen in equations 3.4 and 3.5. The temperatures of both sensor points are independent of each other and are added up using gaussian square error. In equation 3.5, P is the power added to the system, d is the length of the device under testing, w its width and h its height. ΔT is the temperature difference over the test device.

$$\Delta(\Delta T) = \sqrt{|\Delta T_2|^2 + |\Delta T_1|^2} \tag{3.4}$$

$$\Delta\lambda = \sqrt{\begin{aligned}&\left(\frac{\Delta P \cdot d}{\Delta T \cdot w \cdot h}\right)^2 + \left(\frac{P \Delta d}{\Delta T \cdot w \cdot h}\right)^2 + \left(\frac{P \cdot d}{(\Delta T)^2 \cdot w \cdot h} \cdot \Delta(\Delta T)\right)^2 \\ &+ \left(\frac{P \cdot d}{\Delta T \cdot w^2 \cdot h} \cdot \Delta w\right)^2 + \left(\frac{P \cdot d}{\Delta T \cdot w \cdot h^2} \cdot \Delta h\right)^2\end{aligned}} \tag{3.5}$$

To merge multiple results gained from different power settings, weighted average with inverse errors is used.

3.2.1 Validation of UFO Setup

The UFO was validated for thermal conductivity measurements using a known material, copper, as reference. A 500 µm thick strip of copper, cut into a 25±0.1x80±0.1 mm^2 large rectangle is used as reference sample. Two Pt100 sensors (d=35±2 mm) are applied to the sample. For thermal input, a flexible kapton heater of area 1x1 in^2 is mounted onto the copper strip. The entire strip is coated with black spraypaint for high and uniform emissivity. This strip is mounted into the heatsink (see fig. 3.12). The UFO is put under a moderate vacuum of 0.025 mbar. Measurements are taken with powers between 0 W to 5 W at 0 °C and -20 °C in 1 W increments. The measurements were taken 2-3 minutes after adjusting the thermal input to give the system sufficient time to reach equilibrium. The Pt100 sensors were read out using a custom program, while the camera was read out using the IRBIS 3Plus software using the "record snapshot" feature, generating a series of 1200 images at 60 Hz (reference image see fig. 3.11). Then using the software, the marked points on the image were converted into a tabularized list of temperatures. The data was cleaned and imported into OriginLab for processing.

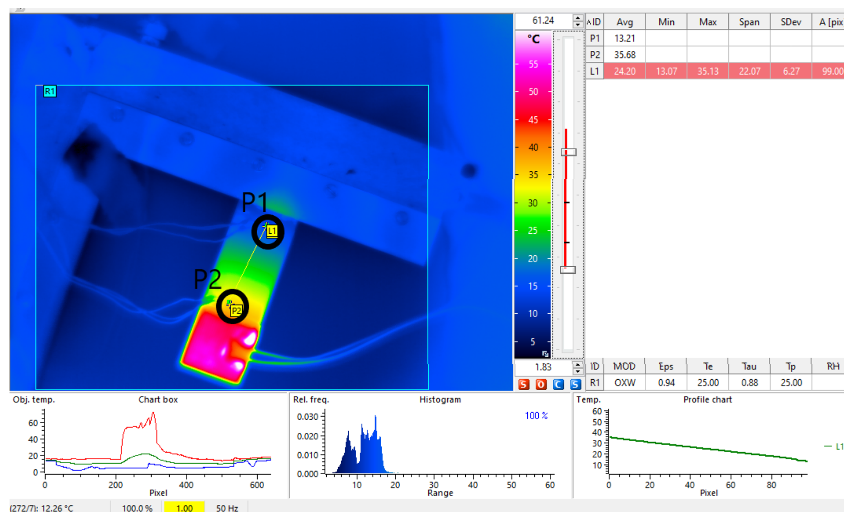

FIGURE 3.11 –

Infrared picture of the copper strip at P=3 W. The heater shows high temperatures with a gradient on the copper strip itself. Measurement points 1 and 2 are placed on the sensors for reference. Bottom right above the graphs displays the calibration settings input for this measurement.

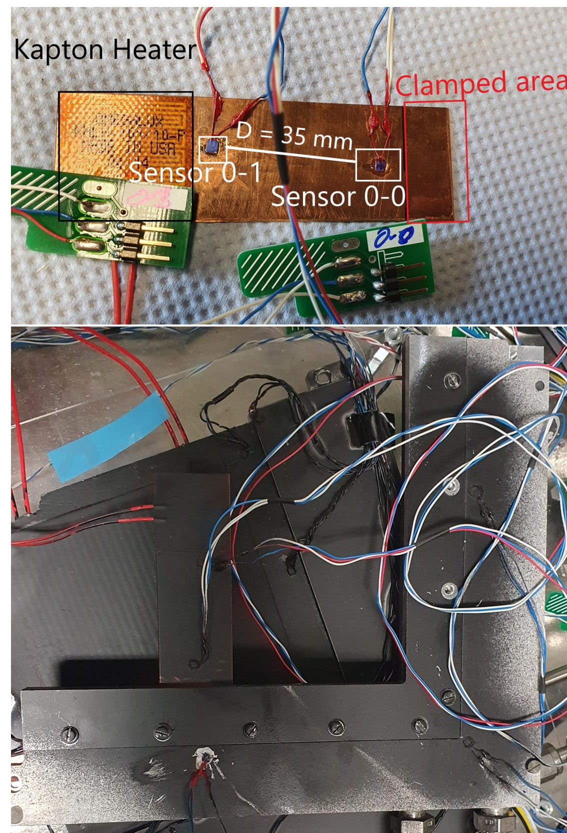

Figure 3.12 –
Top: The copper sample without spraypaint. Visible are the Kapton heater and the sensors glued onto the copper strip. Bottom: The copper sample spraypainted black for even emissivity and clamped in the heat sink.

3.2.1.1 Results

Fig.3.13 shows the ΔT measured across the sample. The ΔT can now be used with the sample dimensions to calculate λ (eq. 3.2) for each power value and then averaged using weighted averages (see fig.3.14) for λ_{Cu} over the averaged temperature. The results are shown in table 3.2. This provides validation to usability of the UFO and the selected sensor setup. The next step is to measure samples of both TPG and PGS/RVC, to validate their thermal properties and measure their λ. This can then be used to simulate the thermal properties of a full module.

Environment/ $T_{Coolant}$	**Sensor**	λ in $\frac{W}{m \cdot K}$	T_{Range}
0 °C	Pt100 sensors	400 ± 10	1.8-36.8 °C
	IR camera	390 ± 10	1.8-36.8 °C
0 °C	literature	401	

Table 3.2 –
Weighted average results of the thermal conductivity of copper. T_{Range} denotes the range of temperatures of the measured points that are combined into the displayed λ_{Cu}.

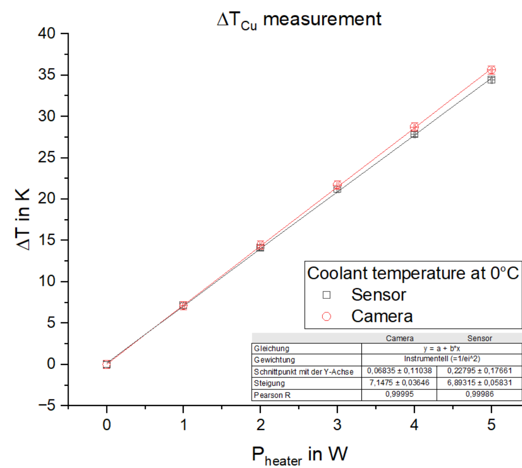

FIGURE 3.13 –

Copper measurement at 0 °C coolant temperature. ΔT of sensor and camera.

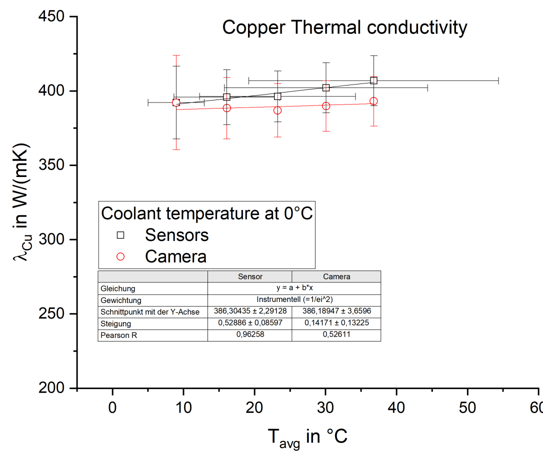

FIGURE 3.14 –

λ_{Cu} over the averaged temperature of each point. The X-error is used to designate the range around the averaged temperature, with the left end being the lowest and the right end being the highest temperature.

3.3 Material Validation

Each material/composite is tested in a standardized process to validate its thermal conductivity. Each sample is cut into an $8 \times 2.5\,\text{cm}^2$ long strip and equipped with two Pt100 sensors. The procedure used for copper is repeated with TPG and PGS samples (fig. 3.15 and 3.16) and different parameters (see table 3.3).

To produce the PGS/RVC sample, a strip of RVC and PGS were cut out. The glue used was T7110 by Epo-Tek [Epo] due to its availability. The glue was absorbed into a single ply sheet of tissue as a stand in for carbon fleece, which was proposed by the ALICE ITS3 upgrade group. The three pieces were then placed on each other RVC-tissue-PGS and weighed down with a block of Aluminium. The assembly was then placed in an oven at 80 °C overnight to cure the glue. The finalized sample is shown in fig. 3.16.

Parameter	TPG	PGS/RVC
h in µm	380	40(PGS) 2000(RVC)
w in mm	25±2	25±2
P_{max} in W	5.5	3
d_{Sensor} in mm	35 ± 2	36 ± 2
$T_{Coolant}$ in °C	-20, 0, 20	

Table 3.3 –
The table contains the list of varying parameters between each test strip measurements.

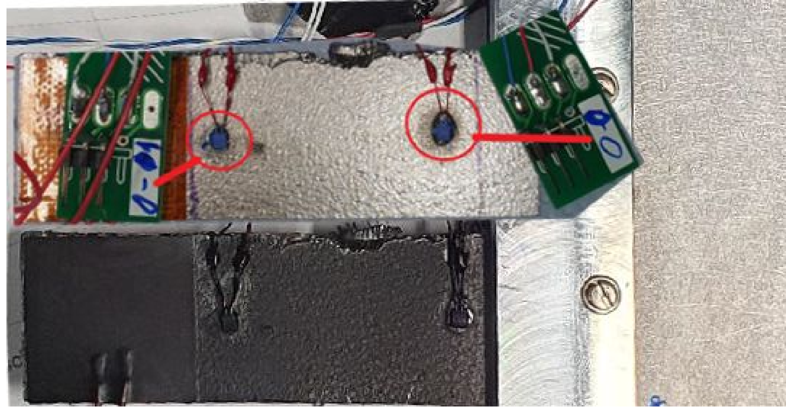

Figure 3.15 –
Top: TPG sample without spraypaint with highlight of the sensors. The kapton heater is visible under the 0-1 board. Bottom: TPG sample spraypainted for uniform emissivity and clamped in the heatsink.

Figure 3.16 –
Left: The front of the PGS/RVC sample. On the left side of the sample the ply sheet is visible.
Right: The bottom of the PGS/RVC sample. Visible is the RVC and the glue (top) in the clamping area used to reinforce the foam structure.

3.3.1 Results

After measurement, the temperature difference ΔT was plotted against P_{heater} (e.g. fig. 3.17). Using eq. 3.2 the λ are computed for TPG and PGS based off each measurement point. These then were plotted against T_{avg} (of the given measurement point) in fig. 3.18. To arrive at T_{avg}, T_1 and T_2 were averaged out and the x-error bars were used to denote the temperature range of each point.

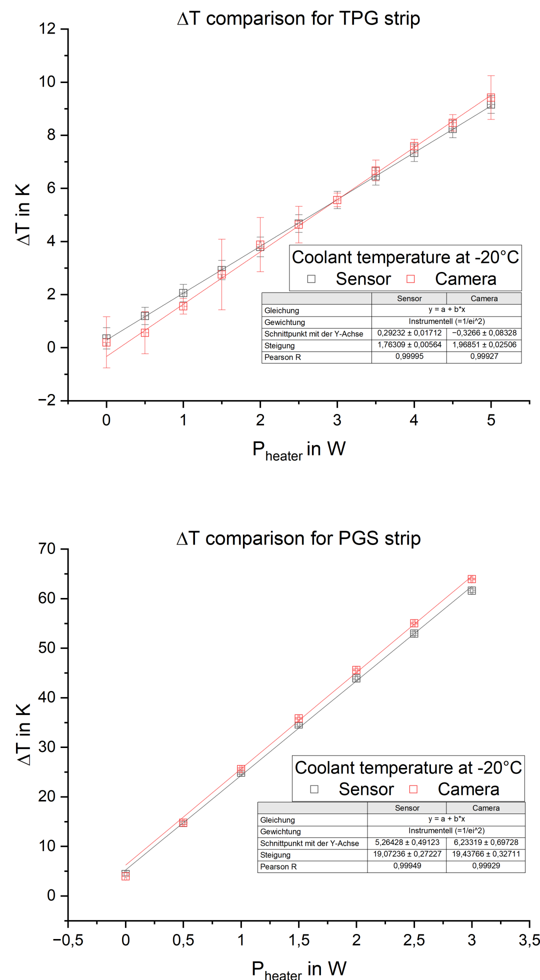

FIGURE 3.17 –

Temperature difference ΔT vs. power for the measurement at -20°C coolant temperature measured with Pt100 sensors and camera for TPG (top) and PGS (bottom) strips.

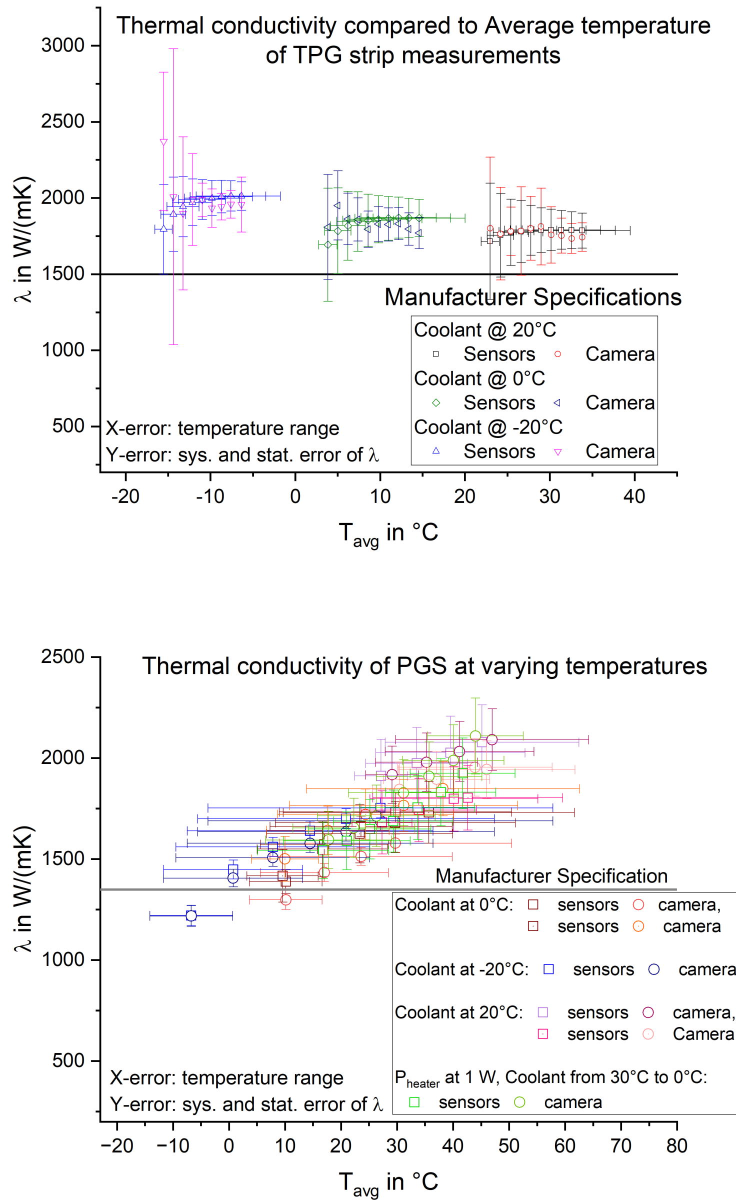

Figure 3.18 –

Thermal conductivity vs. the average temperature of each measurement point. The X-error is used to show the range of temperature between the hottest point on carrier and the coldest of each point. Top: TPG. Each measurement is clearly separated as the thermal transfer is highly effective. Bottom: PGS. It shows that all measurements blend over each other due to the high average temperature and poor effective thermal transfer due to the thin thermal channel.

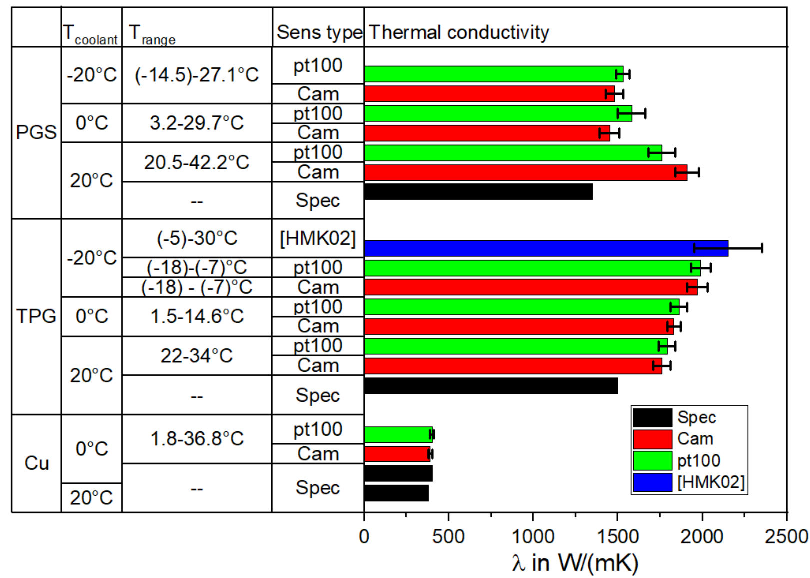

FIGURE 3.19 –

The thermal conductivities of copper, TPG and PGS compared. While the conductivity measurements for copper agree with literature, the measurements done for both PGS and TPG exceed the ones given by the manufacturer. For TPG an additional paper was found that corroborates these findings [HMK02], which did measurements at -17 °C and in moderate vacuum with a comparable sample piece.

Source	λ in $\frac{W}{m \cdot K}$	
	TPG	**PGS**
20 °C		
Pt100 sensors	1790 ± 50	1760 ± 80
IR camera	1760 ± 50	1910 ± 70
literature	1500	1350
0 °C		
Pt100 sensors	1830 ± 40	1450 ± 60
IR camera	1860 ± 50	1580 ± 80
-20 °C		
Pt100 sensors	1970 ± 60	1480 ± 50
IR Camera	1990 ± 60	1530 ± 40
[HMK02]	2150 ± 200	

Table 3.4 –

Weighted average results of the thermal conductivity for TPG and PGS.

From this the thermal conductivities are extracted as shown in graphic 3.19 and table 3.4. The value for [HMK02] was extracted from figure 3.20, the graph 1b in the cited paper. Specifically the data for "Advanced Ceramics" was compared as from reading the data in the paper, it seems

to have been closest to the used sample in this thesis. Of note is that Heusch and Kholodenko measured a strip of their material in a vacuum in a similiar setup as done in this thesis.

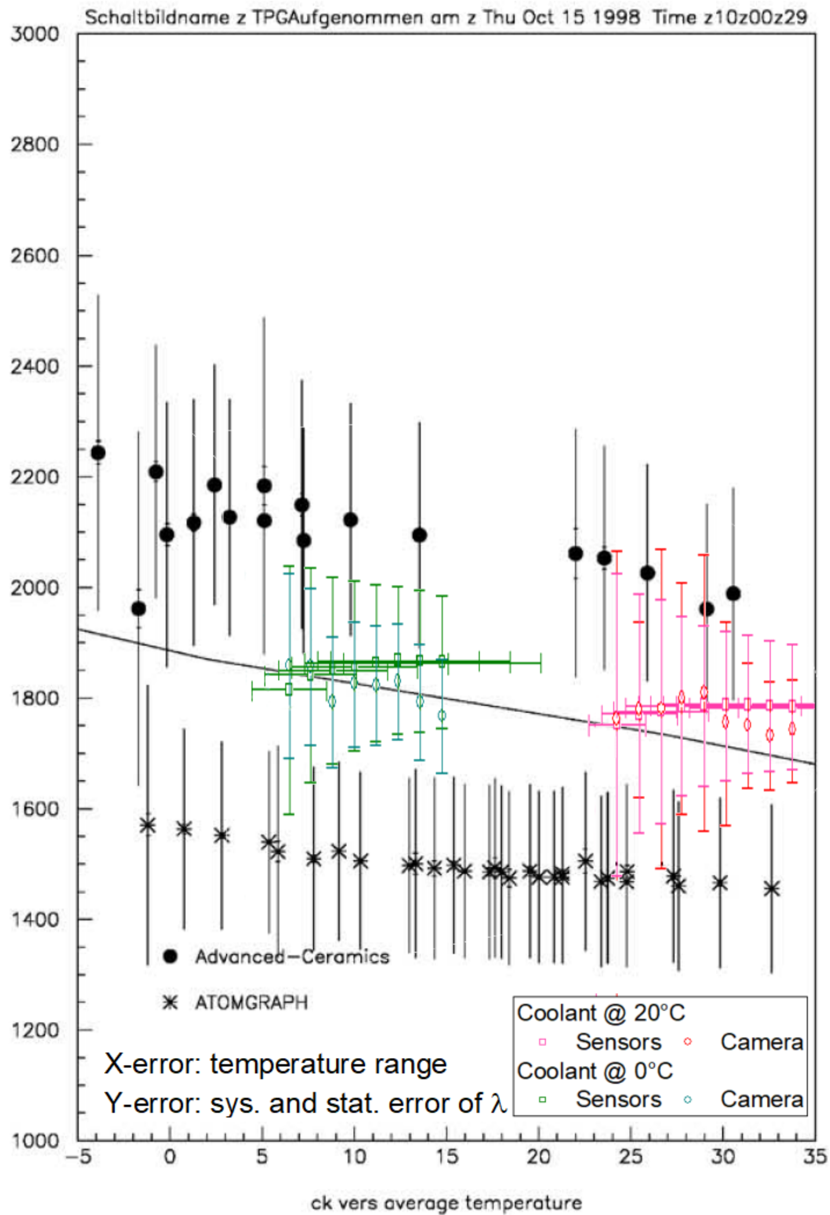

Figure 3.20 –

The thermal conductivity of TPG as measured by C.A. Heusch and A. Kholodenko [HMK02]. Of interest is the dot measurements "Advanced-Ceramics" as it it closest to the used material as described by Heusch and Kholodenko. Measurements for TPG have been added, scaled to the graph.

3.4 Thermal Simulations using ThSim

ThSim is an application modification programmed by Markus Greither [Mar] for electric circuit simulation software LTSPICE XVII [Ana]. It takes advantage of the similarities between electric conductivity mathematics and thermal conductivity mathematics to make a free, simple simulation software for thermal properties. It is limited in scope to simple shapes and isotropic materials. Combining several quadratic shapes allows for the creation of more complex shapes like a L-shaped heatsink. The goal is to first tune the ThSim simulations using measurements of the thermal conductivity and use the resulting settings to predict the thermal performance of a full size station geometry c quadrant as described in [SD22] as well as discuss the different options outlined in 2.1. Initially the results from material validation (ch. 3.3 and onward) are used to tune ThSim, then the different carrier options (see ch. 2.1) are simulated and compared. This defines the options that are to be looked at further and physically tested with a full scale carrier.

3.4.1 Aligning Simulation Parameters to Reference Measurements

For aligning the simulation with the measured results, the TPG strip (see ch. 3.3) is reconstructed in ThSim. A strip of 8 cm length and 2.5 cm width with a 2.5 by 2.5 cm^2 large kapton heater is simulated. The heat entry is set to 5 W. The thermal conductivity of TPG is set to 1500 and 1950 $\frac{W}{m \cdot K}$ respectively to simulate literature and the measured conductivity. The heatsink and environment are set to 0 °C. The simulation is then compared to the measurements performed in ch. 3.3.1.

Fig. 3.21 compares the location of the sensors used in the strip measurements (ch. 3.3) to the ThSim simulations of a TPG strip. The resulting ΔT is shown in table 3.5. From it the simulation tuned to the thermal conductivity of 1950 $\frac{W}{m \cdot K}$ produces an accurate result and therefore λ=1950 $\frac{W}{m \cdot K}$ will be used from here on to simulate TPG.

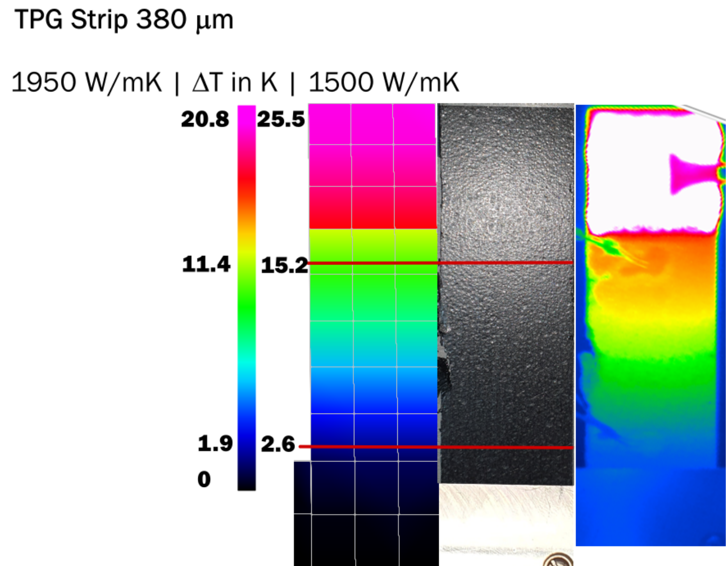

Figure 3.21 –

The unpainted TPG sample compared to a thermal image under load and a simulation of the strip in ThSim. Left of the color gradient is the tuned ΔT values and right is the untuned values. Visible is the rip in the material on the left hand side due to (at the time) improper cutting technique. The reduction in thickness is taken into account by a larger error in width. The red lines denote the points where sensors are placed on the sample (also visible in the infrared image). The infrared image shows the heater active, with the sensor placement faintly visible. The glue around the sensors is also visible as slightly warmer islands on the sample due to its lower conductivity.

Source	Position 0-0 in ˚C	Position 0-1 in ˚C	ΔT in K
Measured	8.5±0.2	18.4±0.2	9.9±0.3
Sim 1500 $\frac{W}{m \cdot K}$	2.6	15.3	12.7
Sim 1950 $\frac{W}{m \cdot K}$	2.1	11.6	9.5

Table 3.5 –
Comparison table of each sensor position (fig. 3.21). Of note is the higher temperature at each sensor point for the measurement, stemming from an improper connection to the heatsink. In ThSim this connection is assumed perfect and has no thermal delta. The thermal delta across the sample compares to the simulation run at 1950 $\frac{W}{m \cdot K}$(tuned).

3.4.2 Simulations

Initially station geometry c is simulated with a TPG carrier of 380 μm thickness. 16 sensors at the front and 12 sensors on the back are placed in rows of 4 as shown in 2.1. The simulation is done for both 1500 and 1950 $\frac{W}{m \cdot K}$, as seen in fig. 3.22. A uniform power density of 200 $\frac{mW}{cm^2}$ is used in figure 3.22, it has also been simulated for 50, 100 and 150 $\frac{mW}{cm^2}$. T_{env} is set to 0 °C as it only changes the initial temperature in ThSim and does not replicate environmental effects. Of interest is the largest gradient across from the tip of the carrier to the edge inside the corner of the heatsink. **From here on out, ΔT is measured from the two furthest points on the carriers.**

When comparing simulations of differing power densities, one notices that the temperature scales linearly on each point, as such ΔT also scales linearly. This helps with comparing simulations of different power densities as they only need to be linearly adjusted. Of note as well is that each simulation is very uniform in behaviour, as ThSim cannot simulate more complex real life cases. As such, heating from other sources and potential uneven thermal dissipation cannot be taken into account. This limits the scope of its use, but it does give a good understanding of viability of each option.

In fig. 3.23, a sample simulation of each carrier option is shown. The outcomes of these simulations are summarized in table 3.6 and figure 3.24. This shows that options *thinned baseline*, *ladders* and *2xOnesided* are all viable on a simulated basis. The PGS option has a ΔT of 20.6 K at 50 $\frac{\text{mW}}{\text{cm}^2}$ and therefore is not further considered for the *CBM-MVD*. However, PGS/RVC will be discussed later in the discussion, as it has interesting properties in less constrained environments.

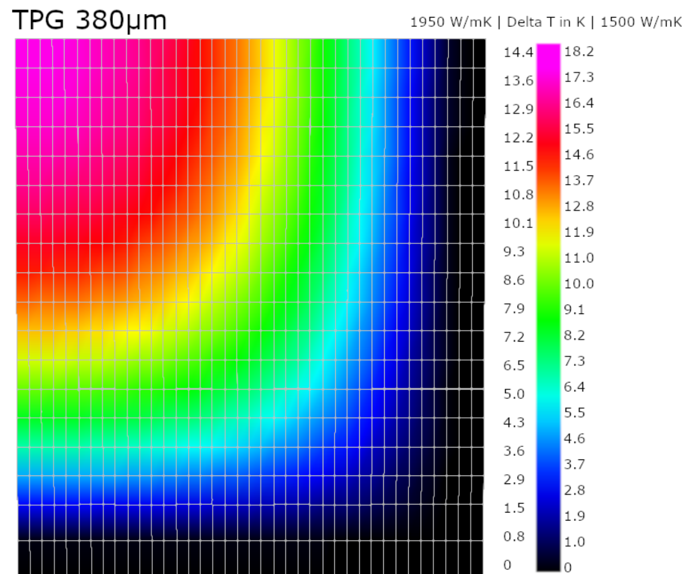

Figure 3.22 –

Top down view of a ThSim based simulation of station geometry c made of TPG (380 µm thickness) for a thermal conductivity of 1950|1500 $\frac{W}{m \cdot K}$ and power density of 200 $\frac{mW}{cm^2}$. The individual sensors are not visible in the simulation after relaxation period, showing the high high performance capabilities of TPG. The left column of numbers is a tuned simulation, the right are untuned values.

Option Power density	ΔT in K $200\,\frac{\text{mW}}{\text{cm}^2}$	ΔT in K $50\,\frac{\text{mW}}{\text{cm}^2}$
Baseline (1950 $\frac{\text{W}}{\text{m}\cdot\text{K}}$)	14.4	3.6
Baseline (1500 $\frac{\text{W}}{\text{m}\cdot\text{K}}$)	18.2	4.55
Thinned Baseline	21.5	5.3
2xonesided (150 µm)	20.5	5.1
Ladders	20.4	5.1
PGS/RVC	82.2	20.6

Table 3.6 –
A Comparison table of each simulated option based on their maximum ΔT. The values are from simulations run at 200 $\frac{mW}{cm^2}$ power density as well as 50 $\frac{mW}{cm^2}$.

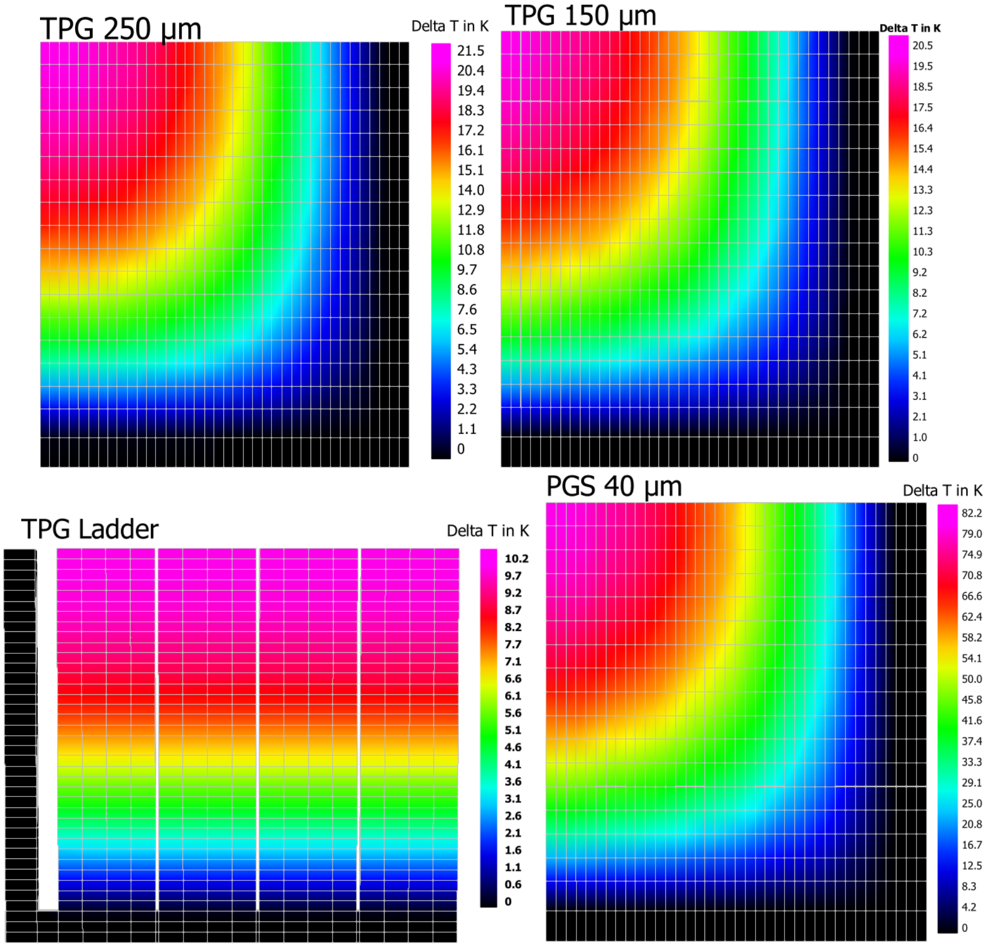

Figure 3.23 –

Top down view of a ThSim based simulation of alternative station c designs. Top left: 250 µm TPG, 200 $\frac{mW}{cm^2}$. Top right: 150 µm TPG, 200 $\frac{mW}{cm^2}$. Bottom left: TPG ladders, 380 µm thickness, 100 $\frac{mW}{cm^2}$. Bottom right: PGS 40 µm thickness, 200 $\frac{mW}{cm^2}$.

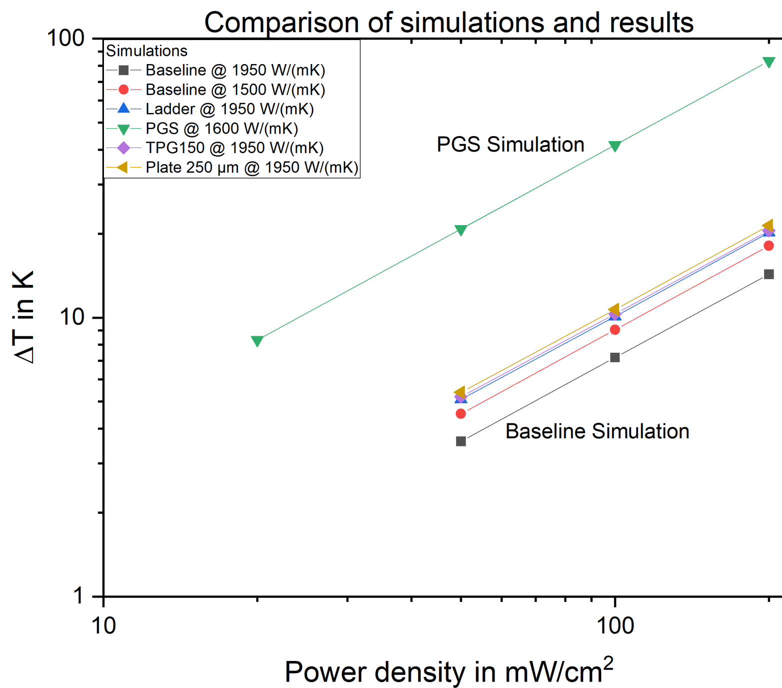

Figure 3.24 –

Each simulated option compared for different power densities. Visual aid lines show the trend of ΔT. The different simulations for TPG cluster together. All simulations point towards the TPG based options all coming in under or around 10 K for ΔT at 100 $\frac{mW}{cm^2}$. The PGS/RVC option at 50 $\frac{mW}{cm^2}$ is at twice the benchmark set for this thesis and is therefore not considered further for CBM-MVD.

3.4.3 Comparison to High Fidelity Simulations

A *baseline/thinned baseline* carrier option was simulated using Autodesk Inventor Nastran, an industry standard simulation tool for mechanical and thermal simulations. Inventor Nastran can also simulate anisotropic materials, allowing for simulating the impact of anisotropy on the measurements. The resulting simulations in fig. 3.25 will be compared to the measured values as well.

The simulations were performed at 100 $\frac{\text{mW}}{\text{cm}^2}$and a conductivity of 1500 $\frac{\text{W}}{\text{m}\cdot\text{K}}$in isotropic and anisotropic version. Comparing the resulting ΔT between Nastran and TSim for 1500 $\frac{\text{W}}{\text{m}\cdot\text{K}}$ and 380 µm, both simulation programs broadly agree (see fig. 3.7). This confirms that ThSim is usable for this working case. Additionally the difference in Nastran between isotropic and anisotropic is negligible (see fig. 3.25, left and right).

Option	ThSim	Nastran
	Δ T in K	
Baseline	9.10	9.05
Thinned Baseline	13.9	13.3

Table 3.7 –

A Comparison table of ThSim and Inventor Nastran for baseline and thinned baseline at $\lambda = 1500 \frac{W}{m \cdot K}$ *and* $100 \frac{mW}{cm^2}$.

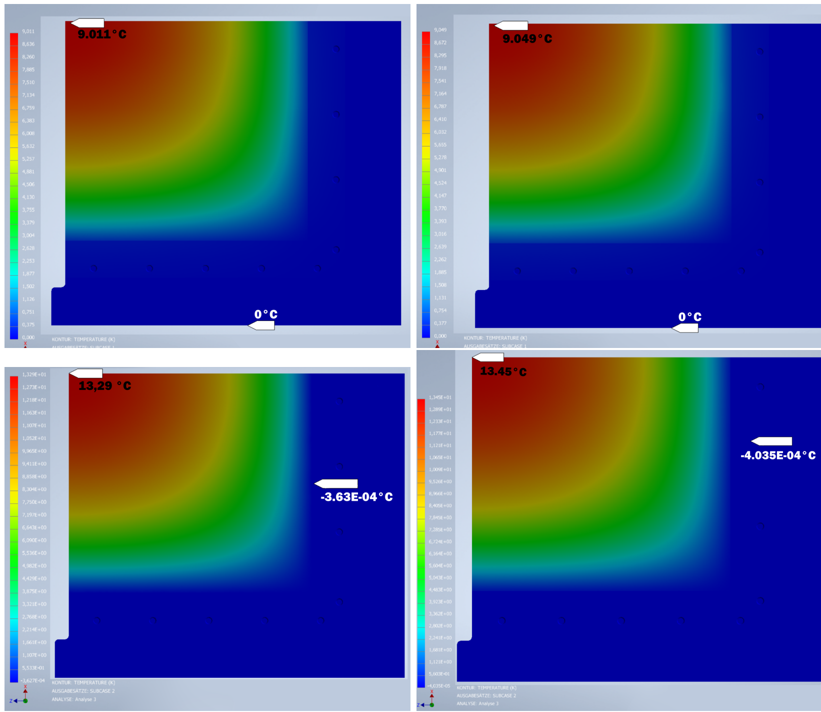

FIGURE 3.25 –

Top down view of a Autodesk Inventor Nastran based simulation of station geometry c (thinned) Baseline [F.M]. The carrier size is 140x127 mm^2*, with 130x117.5* mm^2 *in acceptance (v 2.5 of the heatsink), 16+12 sensors with a power density of 100* mW/cm^2.

Top: 380 μm*, Bottom: 250* μm*. Thermal conductivity of 1500 (15)* $\frac{W}{m \cdot K}$ *isotropic (anisotropic z-direction).* T_{env} *set to* $0\,^{\circ}C$.

3.5 Carrier Measurement

Measurements of a 380 µm and 250 µm thick carrier were performed in 10 K steps from -30 °C up to 20 °C in hysteresis. The heating was provided by kapton heating elements and the heating power was varied from 0 to 20 W in steps of 2 W. The clamp screws were tightened to 0.4 Nm to achieve a good thermal contact between the carrier and heatsink. The vacuum pressure, carrier sizes and other parameters are listed in table 3.8. Images of the samples are shown in fig. 3.26. The carrier sizes were measured and written down in table 3.8. The *baseline* carrier had damage at the outer corner, moving the heater seven mm closer to the heatsink (see fig.3.26 left).

Parameter	380 µm carrier	250 µm carrier
P_{Vac} in mbar		$250 \cdot 10^{-5}$
Sensors	IR Camera & Pt100	Pt100
Size in cm^2	13.7*x*12.8	14.4*x*12.7
Heaters	Kapton (front/back)	Kapton (back)
T_{Room} in °C	15-20	15-25

Table 3.8 –
Experimental parameters for the carrier experiments.

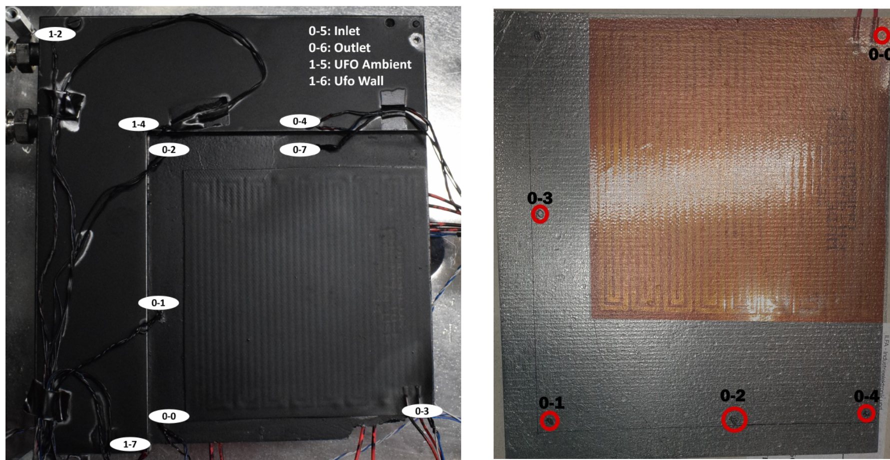

Figure 3.26 –

Each Pt100 sensor is marked with its labeled number in the system, 0-x denoting sensors read out on board 0, 1-x denoting sensors read out with board 1.

Left: Baseline option sample clamped inside the heat sink. The sample already has been spray-painted for even emissivity. The damage on the carrier forced the heaters to be mounted slightly lower, making the distance to the heat sink equal in both directions.

Right: Thin carrier option sample. A front and back picture were overlayed to show where the heating pad is situated on the carrier bottom. The sensor positions are marked with red circles.

3.5.1 Discussion Carrier Experiment

The temperature difference ΔT across the carriers is compared to the simulations (see fig. 3.27). Comparing for baseline (black, brown) and thinned baseline(red, light blue) they agree within two to three K (see tab. 3.9). The discrepancy could be due to influences from any of the factors discussed in ch. 3.1.8 and needs examination.

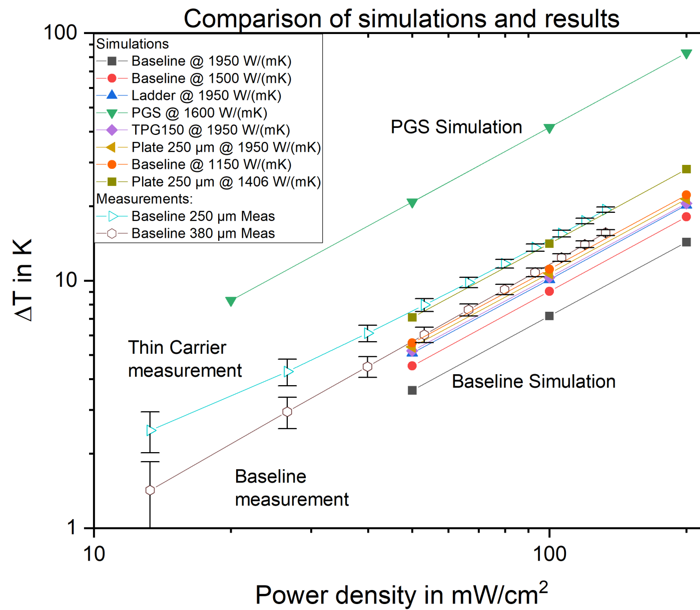

FIGURE 3.27 –

Each simulated option compared for different power densities. The lines are "guide the eye", not calculated. A log-log visualization is used as the PGS simulations increase the range to a point it makes distinction between TPG simulations impossible. The results of the carrier measurements are included, showing that the simulations overestimate actual λ. Simulations tuned to λ ~ 1150$\frac{W}{m \cdot K}$ for Baseline and λ ~ 1406$\frac{W}{m \cdot K}$ for thin baseline were added based on results from eq. 3.8.

The thermal contact between the heater and the carrier may not be perfect. This is unlikely as it would lead to overestimation of thermal conductivity, not underestimation like in this case. The carrier size between *baseline* and *thin baseline* only changes in the z- direction and stays the same within each data set. Of note is the given carrier sizes in table 3.8. The tip of the *baseline* carrier is damaged. As such ~seven mm are missing off the carrier (see fig. 3.26). The simulations use the same carrier sizes (see table 1.2 station geometry c.) as this small defect cannot be accounted for in ThSim.

It is also prudent to understand the contact between the heat sink and the carrier. This mainly influences total temperature and less the ΔT across the carrier. When comparing measured temperature differences between the heatsink and the carrier with calculated differences as seen in fig. 3.7 one finds a higher ΔT for the measurements compared to theory. This was calculated based off $100 \frac{mW}{cm^2}$ (ca. 15 W total for all sensors) as done in ch. 3.1.7 and is compared to the measured values at 16 W on the baseline carrier sample. The thermal difference for the calculation is $\Delta T \sim 1.14$ K, whereas the measured value is $\Delta T \sim 1.4...1.8 \pm 0.4$ K, depending on coolant temperature.

Another error source could be the Pt100 sensors-carrier contact. It could contain too much glue under one or more sensors, decreasing the sensor accuracy. This is minimized by using as little glue as necessary and keeping pressure up on the sensor throughout the entire curing process.

A difference between the top and bottom can be ruled out based on fig. 3.9, which was taken off the baseline carrier. As the other carrier is thinner, the same can be applied there as well. Lastly, the measurements can be corrected for the thermal input of the environment in two ways:

1 1/x analysis

2 P_{env}, Stefan-Boltzmann correction

Correction 1 is based on the idea that, with increasing power from the heaters, the additional entry from the environment turns negligible. As such the fraction of ΔT and P_{total} should converge to the clean relation between ΔT and P_{heater}. This is plotted against P_{total}. The function $A + B/x$ is then fitted. Parameter A, the y- offset of the convergence point then corresponds to the gradient of the ΔT - P_{total} function.

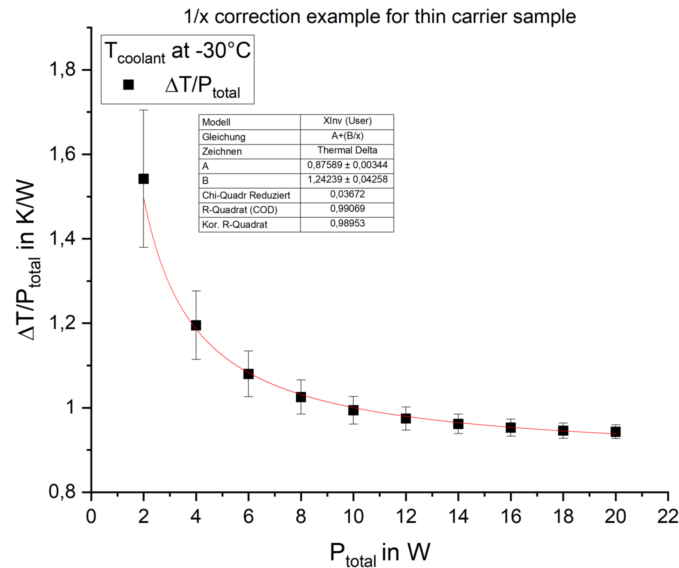

FIGURE 3.28 –

Graph example for the 1/x method done at $T_{coolant}$=-30°C. ΔT is divided by P_{total} and plotted against P_{total}. The resulting curve corresponds to $A + B/x$ and A corresponds to the gradient of ΔT-P_{total}.

The resulting gradient is $g_{1/x}$=0.876 ± 0.004.

Conversely correction 2 subtracts the environmental heat entry from P_{total}. For this eq. 3.3 is used as in ch. 3.1.8 and subtracted off P.

Both corrections can then be plotted together with the original data to compare, see fig. 3.29.

This results in a gradient of g_{SB}=0.912 ± 0.005. Correction 1 shifts the data down to start at $\Delta T = 0$, but does not change the gradient (g_{uncorr}= 0.873 ± 0.004 to $g_{1/x}$= 0.876 ± 0.004). Correction 2 on the power changes the gradient and moves the graph. Primarily lower power measurements are affected as with increased power the relation between $P_{environment}$ and P_{heater} becomes dominated by the heating power. This correction under corrects as of now, not being able to shift the y-axis intersection to 0. This points at an additional shift needed to achieve a full correction. The relative change in gradient for the Stefan-Boltzmann correction corresponds to a 5% change, while the change using the 1/x correction corresponds to 0.4%. As such they cannot account for the large discrepancy between strip and carrier measurements.

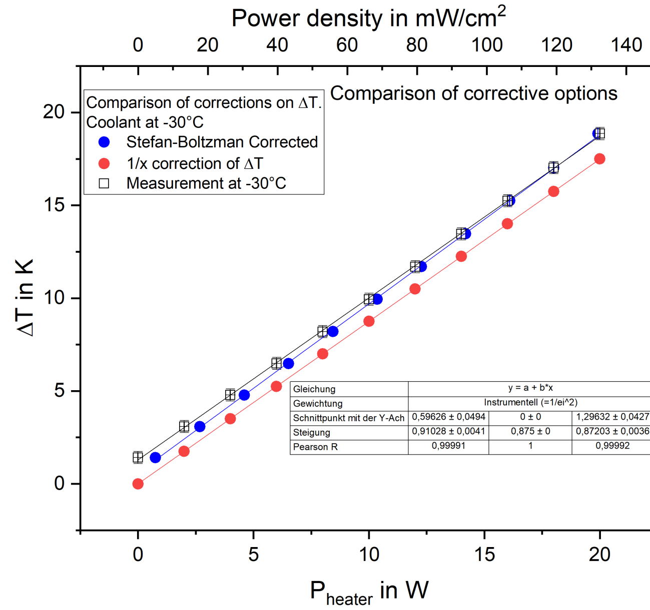

FIGURE 3.29 –

Comparison of two correction methods applicable to measurement data. One correction is applied to ΔT and the other correction can be applied to P. In this example it was done to a measurement of the thin carrier at -30°C coolant temperature to compare with the largest $P_{environment}$.

$$\lambda_{meas} = \frac{Q \cdot l}{A \cdot \Delta T_{meas}}, \lambda_{meas} \Delta T_{meas} = \frac{Q \cdot l}{A} \tag{3.6}$$

$$\lambda_{sim} = \frac{Q \cdot l}{A \cdot \Delta T_{sim}}, \lambda_{sim} \cdot \Delta T_{sim} = \frac{Q \cdot l}{A} \tag{3.7}$$

$$\lambda_{meas} = \frac{\lambda_{sim} \cdot \Delta T_{sim}}{\Delta T_{meas}} \tag{3.8}$$

The significant discrepancy between the tuned carrier simulations based on sample measurements and the carrier measurements cannot be adequately explained by errors in the process. A simple calculation can be used to create a “reference” conductivity for the carrier measurements. For this, it is assumed the power applied in simulation and measurement is equal, as are the physical proportions of the carrier. This assumption results in eq. 3.8. Table 3.9 contains the λ of baseline and thin option as gained from the simulation and strip measurements as well as the λ as obtained through eq. 3.8. The resulting λ_{meas} is then used to simulate the carrier options again and is added into fig.3.27.

Parameter	380 μm carrier	250 μm carrier
λ_{sim} in $\frac{W}{m \cdot K}$	1950	1950
ΔT_{sim} in K	4.78	7.11
ΔT_{meas} in K	8.10±0.40	9.86±0.24
λ_{meas} in $\frac{W}{m \cdot K}$	1150±70	1406±35

Table 3.9 –
λ_{sim} compared to λ_{meas}. The measurement is based on Q= 10 W, $T_{coolant}$= 0 °C. The temperature difference ΔT_{sim} of the simulation was adjusted to 10 W as it scales linearly.

Summary 4

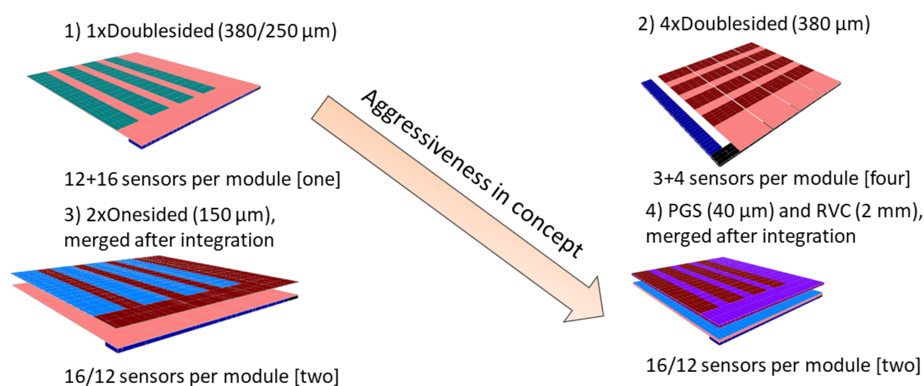

Figure 4.1 –

Visual representation of options discussed in this thesis, done with ThSim. Top left: Baseline and thinned baseline (1xDoublesided). Top right: Ladders (4xDoublesided). Bottom left: 2xOnesided TPG. Bottom Right: PGS/RVC composite (2xOnesided). The top and bottom are separated to show the idea behind the 2xOnesided concepts.

The **M**icro **V**ertex **D**etector is part of the CBM experiment for FAIR SIS 100. It encompasses four stations placed in vacuum behind the target to measure tracks of charged particles emitted from heavy ion collisions and proton induced reactions.

Currently the MVD is in a transition phase from R&D to production. The baseline material for MVD production is carbon based Thermal Pyrolitic Graphite (TPG). The TPG sheets provide cooling and mechanical stability for the sensors in use inside the geometric acceptance.

In this thesis, the possible production yield of the MVD station geometry c module has been discussed (ch. 2.2.7). The discussion was focused mainly on the conceptual part as no statistical numbers are available. A high production yield is only achieved by optimizing and perfecting each step in the construction process (e.g. sensor integration, gluing and bonding of FPC cables, clamping in heatsink, merging two modules). Additionally the need for robust QA, high quality work and the ability to rework components was highlighted as integral part for a successful volume production of MVD stations (fig. 2.6). New possible construction variants (*thinned baseline, ladders, 2xOnesided*) and material options (**P**yrolitic **g**raphite **s**heet/**R**eticulated **v**tireous **c**arbon foam, PGS/RVC composite) were then compared on material budget as well as thermal management perspective. The resulting discussion highlights pros/cons of the alternative options and compares them to the current *baseline* for MVD.

The thermal properties of the chosen materials TPG and PGS/RVC compound were validated. The results were then used to tune simulations of different MVD carrier options performed with ThSim and Inventor Nastran to evaluate their usability for the CBM case. These simulations were then compared to measurements done for *baseline* and *thinner baseline* carriers where ΔT measured across the carrier was used as a benchmark. For the MVD construction it is stated that the ΔT should not be larger than 10 K, however, this is not a strong limit. The results of the measurements and simulations are compared in table 4.1. They agree with each other within some K, strengthening the use case for simulations models to approximate the thermal performance of complex objects such as the MVD quadrant. The *thinned baseline* option can be considered for use in the MVD as it reduces the material budget by 10% per station b/c. The discrepancy of measurements leading to the tuned simulations and the carrier measurements requires further investigation. It could not be addressed in this thesis due to time constraints.

If less material budget is needed, the carrier can be thinned to 250 µm without significant loss of structural integrity. The option *2xOnesided* also imparts a minor saving of material budget but it is not its main selling point.

	380 μm carrier	250 μm carrier
Simulations		
ΔT_{1500} in K	9.05	13.9
ΔT_{1950} in K	7.2	10.7
$\Delta T_{meas,sim}$ in K	11.1	14.1
Measurements		
ΔT_{meas} in K	12.4 ± 0.5	15.5 ± 0.5

Table 4.1 –
ΔT based on tuned simulations done at $100\frac{mW}{cm^2}$ for $\lambda \sim$ 1500, 1950 $\frac{W}{m \cdot K}$ compared to measurements done on baseline and thinned baseline carrier. $\Delta T_{meas,sim}$ denotes the temperature difference if ThSim is tuned to λ_{meas}.

The focus of this thesis was also on investigating carrier options with higher modularity. It is of interest for reducing amount of material that is discarded due to failure of a module. Two options with similar material budget to baseline were considered. Option one (*2xOnesided*) separates the double sided integration into two single sided integrated modules. The other option (*Ladders*) subdivides the carrier into four double sided modules (see both options in fig. 4.1 top right, bottom left). In terms of thermal performance, in simulations both options do not suffer from a large degradation in performance compared to baseline. They are capable of efficiently transferring the heat into the heatsink. While the 2xOnesided module is relatively simple to build, care has to be taken when marrying both sides with the heatsink to align them properly. The Ladders concept is of higher risk as the FPC cables will have to be routed perpendicular to four independent ladder fingers. This may result in a reduction of production yield.

The thermal performance of the PGS/RVC carrier was evaluated to be insufficient for the MVD use case. Additionally the material budget reduction was less than expected due to the amount of additional glue required.

Appendices 5

5.1 Bent TPG Measurement

A measurement of a TPG strip is done after bending it 90°. The bend is placed between the sensors, to measure a potential loss of conductivity after mechanical damage. The bend is shown in fig. 5.1. Of note is that there is no ripping visible in the picture nor anywhere else on the material, pointing towards a delamination of the layers of carbon.

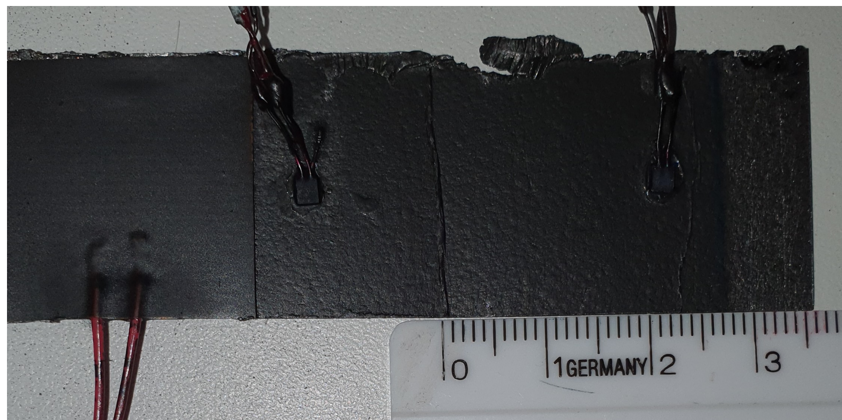

Figure 5.1 –
The damage incurred by bending a strip of TPG 90°. The bend is clearly visible as a "welt" on the strip.

A measurement like in ch. 3.3 is performed, up to 5.5 W. $T_{coolant}$ is set to 0 °C. λ_{bent} is calculated at 1920±50$\frac{W}{m \cdot K}$ for the sensors and 1780±50$\frac{W}{m \cdot K}$ for the IR camera. While the data is more

scattered in itself than other measurements, it still points to a higher than manufacturer λ, congruent with the other strip measurements (see table 4.1). Of note is the lower conductivity measured by the IR camera. The camera is possibly miscalibrated. Nontheless, the camera can be used to visually inspect the sample under load in the vacuum, see fig. 5.2. In the image, while a possible discontinuity could be visible in the transition from yellow to green in the area where the bend is, it is also likely that it is just a visual trick of the color gradient. This gives a possible conclusion that material defects, as long as they do not tear the layers, only minorly degrade the thermal performance of TPG. Conversely the mechanical performance is majorly degraded, as the strip could barely keep itself straight with the weight of the

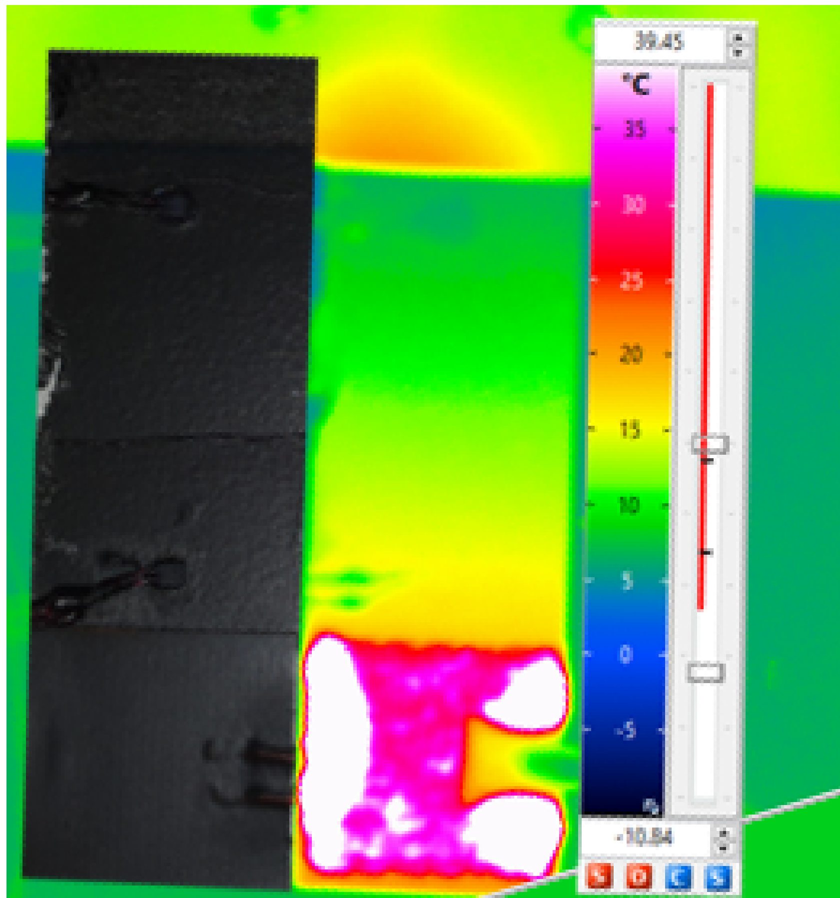

Figure 5.2 –

A thermal image of the bent TPG taken using the IR camera, lined up with a camera image of the bent sample. A possible discontinuity of conductivity could be visible, but it could also be a part of the color gradient, suggesting a discontinuity.

Bibliography

[3M09] 3M. The 3m™ novec™ brand family, September 2009. "3M™ Novec™ 649 Engineered Fluid".

[A+08a] Aad, G. *et al.* The ATLAS experiment at the CERN large hadron collider. *Journal of Instrumentation*, 3(08):S08003–S08003, aug 2008.

[A+08b] Aamodt, K. *et al.* The ALICE Experiment at the CERN LHC. *Journal of Instrumentation*, 3:S08002, 08 2008.

[ABC+07] IC Arsene, LV Bravina, W Cassing, Yu B Ivanov, A Larionov, J Randrup, VN Russkikh, VD Toneev, G Zeeb, and D Zschiesche. Dynamical phase trajectories for relativistic nuclear collisions. *Physical Review C*, 75(3):034902, 2007.

[Ana] Analog Devices. Ltspice xvii, copyright analog devices, inc., 1995-2022. `https://www.analog.com/en/design-center/design-tools-and-calculators/ltspice-simulator.html`. LTSpice is a program to simulate electrical circuits.

[Bra17] Angela Bracco. The nupecc long range plan 2017: perspectives in nuclear physics. *Europhysics News*, 48(4):21–24, 2017.

[BSJL09] RK Bhan, RS Saxena, CR Jalwani, and SK Lomash. Uncooled infrared microbolometer arrays and their characterisation techniques. *Defence Science Journal*, 59(6):580, 2009.

[C+08] Chatrchyan, S. *et al.* The CMS experiment at the CERN LHC. *Journal of Instrumentation*, 3(08):S08004–S08004, 2008.

[C.M] C.Müntz. Personal correspondence with christian müntz. General advice and Boltzmann plot of D-mesons.

[col23] CBM collaboration. Cbm setup at fair, 2023. CAD view of the CBM Setup as shown on the CBm main website, last accessed 18.09.2023.

[Epo] Epo-Tek. Thermal vacuum glue. `https://www.epotek.com/product/t7110/`. Epo-Tek product website for the glue T7110. Last accessed: 09.May 2023.

[ERG] ERGaerospace. Rvc foam properties. `https://ergaerospace.com/carbon-rvc-foam-open-cell-material/`. Website of ERG Aerospace on the topic of RVC foams and their properties.

[FHK+11] Bengt Friman, Claudia Höhne, Jörn Knoll, Stefan Leupold, Jorgen Randrup, Ralf Rapp, and Peter Senger. *The CBM physics book: Compressed baryonic matter in laboratory experiments*, volume 814. Springer, 2011.

[F.M] F.Matejcek. Personal correspondence with franz matejcek. General advice and discussion.

[F.M19] F.Morel. The mimosis-1 architecture., 24-25 June 2019. Presentation shown at the MIMOSIS Design Review, IPHC Strasbourg .

[Han] Hanks, G. How to calculate production yield. `https://bizfluent.com/how-6461493-calculate-product-yield.html`. Article on bizfluent on how to calculate production yield Last accessed: 08.February 2023.

[HMK02] Clemens August Heusch, H-G Moser, and A Kholodenko. Direct measurements of the thermal conductivity of various pyrolytic graphite samples (pg, tpg) used as thermal dissipation agents in detector applications. *Nuclear Instruments and Methods in Physics Research Section A: Accelerators, Spectrometers, Detectors and Associated Equipment*, 480(2-3):463–469, 2002.

[Hö07] Höhne, C. The CBM Experiment at FAIR Exploring the QCD Phase Diagram at High Net Baryon Densities. *International Journal of Modern Physics E-nuclear Physics - IJMPE*, 16:2419–2424, 08 2007.

[Inf] Infratec. Infratec. Vendor.

[Inf15] InfraTec. *Infratec Variocam hr head incl. IRBIS remote 3.0 software description*, 2015. Last opened 15.03.2023. Technical data on p.9.

[Jen] Jenoptik. Jenoptik. Vendor.

[M.A] M.Angeletti. Personal discussion its3. Discussion about use of carbon fleece and gluing procedures at ALICE ITS3 in regards to RVC foam.

[Mag21] Magnus Mager. Presentation on its3 upgrade cern detector seminar, 09 2021.

[Mar] Markus Greither. Thsim temperature simulator, copyright markus greither, 1999-2013, licensed under freeware. https://thsim.sourceforge.net/. A program based on LTSpice software that uses similarities between electrical and thermal equations to approximate a simple thermal simulation software.

[Mat22] Franz Matejcek. Systematic studies on employing novec-649 as the coolant for the cbm micro vertex detector, 2022.

[Mom] Momentive. High conductivity tpg thermal leveler. https://www.momentive.com/docs/default-source/productdocuments/high-thermal-conductivity-graphite-and-composites/momentive-tpg-thermal-levelere5353076cca74ae4ab14be3d44c0a24d.pdf?sfvrsn=fbd97bd2_14. Marketing bulletin of Momentive in regards to Highly Conductive TPG. Last accessed: 07.February 2023.

[Mus19] Luciano Musa. Letter of Intent for an ALICE ITS Upgrade in LS3. Technical report, CERN, Geneva, 2019.

[Nex] Heraeus Nexenos. Tabelle der abweichungen für klasse f 0,3 (b) und f 0,15 (a) nach din en 60751. table of data for the resistance of pt100 sensors by Heraeus .

[Pan] Panasonic. Pyrolitic graphite sheet evolves. http://www1.futureelectronics.com/Mailing/etechs/Panasonic/etechALERT_Panasonic_ThermalManagementSolutions/Panasonic_PGS_White_Paper.pdf. White paper by Panasonic regarding their product line of PGS. Last accessed: 03.February 2023.

[SBB+20] P. Spiller, R. Balss, P. Bartolome, J. Blaurock, U. Blell, O. Boine-Frankenheim, L. Bozyk, M. Chorowski, T. Eisel, M. Frey, T. Giacomini, F. Kaether, H. Khodzhibagiyan, S. Klammes, H. Klingbeil, H.G. Koenig, V. Kornilov, P. Kowina, D. Lens, J.P. Meier, D. Ondreka, I. Petzenhauser, V. Plyusnin, I. Pon-

grac, N. Pyka, V. Raginel, P. Rottlaender, C. Roux, J. Schmidt, M. Schwickert, K. Sugita, A. Szwangruber, P. Szwangruber, R. Trockel, A. Waldt, H. Welker, S. Wilfert, T. Winkler, and D. Winters. The fair heavy ion synchrotron sis100. *Journal of Instrumentation*, 15(12):T12013, dec 2020.

[SD22] J Stroth and M Deveaux. Technical design report for the cbm: Micro vertex detector (mvd). Technical report, GSI-2022-00549, 2022.

[sup22] InfraTec Customer support. Private Communication, 2022.

[Thi09] M. Thirumaleshwar. *Fundamentals of heat and mass transfer.* Pearson Education India, 2009. ISBN 9789332503397, ISBN 9332503397 and ISBN 9788177585193. New Delhi.

[Tis15] Tobias Tischler. *Mechanical integration of the micro vertex detector for the CBM experiment*. PhD thesis, Frankfurt am Main, Johann Wolfgang Goethe-Univ., Diss., 2015, 2015.

[Wer06] Norbert Wermes. Pixel vertex detectors, 2006.

[WO22] R. L. Workman and Others. Review of Particle Physics. *PTEP*, 2022:083C01, 2022. Up to date version of the Review of particle physics, a small booklet from 2014 was used in research.

Acknowledgements

I would like to thank my mother, my dad, my brother and all of my close family for supporting and listening to me while I was working on my thesis. I would like to further thank Christian Müntz, Michal Koziel and Franz Matejcek for being amazing support during the making and writing of the thesis, helping with discussion, concepting and experiments during the thesis as well as proofreading and discussion during writing. I'd like to further thank all my friends who stuck the creation of the thesis with me through the times of COVID and the following crises. I want to thank especially my friends I met through VRChat, giving me a place to relax and discuss.

Selbstständigkeitserklärung

Erklärung nach § 30 (12) Ordnung für den Bachelor- und dem Masterstudiengang: Hiermit erkläre ich, dass ich die Arbeit selbstständig und ohne Benutzung anderer als der angegebenen Quellen und Hilfsmittel verfasst habe. Alle Stellen der Arbeit, die wörtlich oder sinngemäß aus Veröffentlichungen oder aus anderen fremden Texten entnommen wurden, sind von mir als solche kenntlich gemacht worden. Ferner erkläre ich, dass die Arbeit nicht - auch nicht auszugsweise - für eine andere Prüfung verwendet wurde. Frankfurt, den 19.10.2023